Colloids on Patterned Substrates

Clemens Bechinger and Erwin Frey

WILEY-VCH Verlag Berlin GmbH
September 21, 2006

Preface

Two-dimensional layers do not exist as self-contained objects but are often confined to crystalline surfaces. The periodic arrangement of the atoms comprising the substrate provides a periodic external potential for the adsorbed monolayer which must be taken into account to understand the rich phenomenology of experimentally observed phases. In this chapter we will discuss how the phase behavior of monolayers is modified in the presence of substrate potentials with different geometries. Experimentally, this situation is realized by colloidal particles which are interacting with interfering laser beams. In the meantime, this field has attracted considerable attention, both from theory and experiments, because many of the findings can be directly transfered to atomic and molecular systems. This also highlights the use of colloidal particles as model systems for such investigations.

Clemens Bechinger (1), and Erwin Frey (2)

(1) Stuttgart, Germany and (2) München, Germany

Contents

3 Colloids on Patterned Substrates

3.1 Introduction

Soft materials comprised of colloidal particles undergo phase transitions from fluid to crystalline order just as their atomic counterparts (Chaikin and Lubensky 1995; Pusey and van Megen 1986; Löwen 1994; Russel et al. 1995). With sizes comparable to the wavelength of visible light, colloidal systems can be conveniently investigated with optical methods. The intrinsic time and length scales of such suspensions offer the advantage to monitor individual particle trajectories in real space and real time. This is in contrast to atomic systems where e.g. structural phase transitions are typically only observed as ensemble averages as obtained by scattering experiments. Another advantage of colloids over atomic systems is the fact that pair interaction energies can be tailored to meet specific requirements. For example, this can be achieved by variation of the salt concentration of the solvent, the dielectric properties of the particles or by adding polymers to the suspension (Russel et al. 1995; Israelachvili 1985; Likos 2001). Colloids thus constitute fascinating model systems to study material properties. Even new crystalline structures without known atomic analogue have been found (Leunissen et al. 2005) for mixtures of charged colloids.

This review focuses on the phase behavior of colloidal particles confined to two dimensions subject to an external periodic potential, which for example can be realized by interfering laser beams (Chowdhury et al. 1985; Wei et al. 1998), periodic pinning arrays (Mangold et al. 2003), and imprint or stamping techniques (Lin et al. 2000). Two-dimensional (2d) systems often differ not only quantitatively but qualitatively from their three-dimensional (3d) counterparts. This is most strikingly seen in systems where the order parameter shows a continuous symmetry, such as solids on a smooth substrate or magnetic systems described in terms of the XY model. Here a general theorem by Mermin and Wagner (1966) states that thermal fluctuations always destroy any kind of long-range order if interactions are sufficiently short-ranged. Despite this fact there are still phase transitions between solid and fluid phases where the stiffness of the solid phase is lost. The low temperature phase is then characterized by quasi-long-range order (QLRO), where correlations between fluctuations in the order parameter density still decay to zero but only algebraically instead of exponentially as in the fluid phase. The physical mechanism driving the transition has been identified as the unbinding of topological defects such as vortices for magnetic systems and dislocations and disclinations for solids (Berezinskii 1971b; Berezinskii 1971a; Kosterlitz and Thouless 1973; Halperin and Nelson 1978; Nelson and Halperin 1979). For a review of the theory of defect mediated phase transitions the reader may consult a recent book by Nelson (2002). Experiments on melting of colloidal systems on flat substrates are summarized in chapter 2 of this volume by

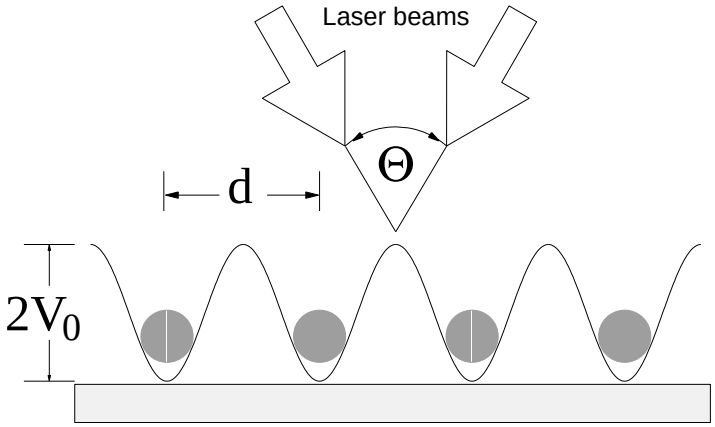

Figure 3.1: Schematic representation of two laser beams which intersect at an angle Θ and form a one-dimensional periodic light potential for colloidal particles as indicated by the solid line. The potential amplitude V_0 is adjusted by the incident laser intensity.

von Grünberg, Keim and Maret. Patterning the surface adds a new feature which leads to an even richer phenomenology with new phases and mechanisms driving the transition between them. For colloidal systems this has first been realized in a series of pioneering experiments by Chowdhury, Ackerson and Clark (Chowdhury et al. 1985). In their studies strongly interacting colloidal particles, confined to two dimensions, were subjected to a one-dimensional periodic potential, induced by the interference fringes from two crossed laser beams; see Fig. 3.1. In the meantime the concept of standing light fields is also successfully applied to Bose-Einstein condensates which allow to probe quantum-mechanical properties of particles on patterned substrates (Bloch 2005). More on the experimental system will be said in section 3.3.4. Starting from a liquid at zero potential strength, $V_0 = 0$, they tuned the periodicity d of the standing wave pattern to a value commensurate with the mean particle distance between the colloids, and observed a phase transition from a fluid into a solid phase upon increasing the laser intensity. This phenomenon has been termed *laser induced freezing* (LIF). Only later, it was experimentally realized by Wei et al. (1998) that the solid phase remelts again at even higher laser intensities (LIM). Since the solid phase is only partially locked by the substrate potential, it is intermediate between a free two-dimensional solid and a density wave on a pattern with full two-dimensional periodicity. While it is pinned transversely to the laser troughs, executing only massive optical phonon-like excitations, it is able to slide freely along the potential minima with acoustic phonon excitations within the troughs. The intriguing phase behavior of such a system, which includes exotic phases like locked and floating solid and smectic phases (Frey et al. 1999; Radzihovsky et al. 2001), will be reviewed in section 3.3.

For three or four laser beams, periodic patterns with two modulation directions can be achieved (Brunner and Bechinger 2002), in particular, square and triangular lattices have been studied (Brunner and Bechinger 2002; Reichhardt and Olson 2002; Agra et al. 2004; Reichhardt and Reichhardt 2005; Šarlah et al. 2005; Šarlah et al. 2006). The colloidal particles then

accumulate in the potential minima thus imposing a modulation of the colloid density. These soft matter systems mimic the behavior found at atomic interfaces, where a prototype role has been played by monolayers of rare gas atoms adsorbed onto the basal planes of graphite (Birgeneau and Horn 1986). These systems are known to exhibit a wide variety of commensurate and incommensurate phases, and have lead to a considerable improvement of our understanding of phase transitions in two dimensions (see e.g. the reviews by Sinha (1980) and Schick (1981) or the book by Lyuksyutov et al. (1992)). The colloidal systems add to this already rich phenomenology the additional advantages of tunability of the substrate potential and the colloid-colloid interaction. For instance, by changing the angles of incidence the lattice constant of the periodic modulation can be varied continuously. Since the electrostatic interaction is usually screened by counterions in the solvent, the lattice spacing also sensitively determines how strongly particles interact. A second route to affect the balance between external compression and internal repulsion is by changing the intensities of the laser beams. Third, the salt concentration of the solvent is a suitable control parameter to tune the range of the repulsive interaction, i.e. the Debye screening length. Fourth, the competition between the attraction to the potential minima and the mutual repulsion of the particles can be conveniently controlled by adjusting the filling factor, i.e., the number of colloidal particles per potential minimum. Exploiting this possibility the potential minima may be filled with "colloidal molecules", thus creating a broad variety of soft molecular crystals.

3.2 Order and broken symmetries in two dimensions

Ordering phenomena in 2d systems are richer and sometimes even genuinely different from the corresponding 3d systems. This is due to a subtle interplay between the enhanced effect of fluctuations and the peculiarities of 2d topology. In particular, there is a clear distinction between models with a discrete and a continuous symmetry. The two archetypical models are the Lenz-Ising (LI) model

$$\mathcal{H}_{LI} = -J \sum_{\langle ij \rangle} S_i S_j \tag{3.1}$$

and the XY model

$$\mathcal{H}_{XY} = -J \sum_{\langle ij \rangle} \mathbf{S}_i \cdot \mathbf{S}_j = -J \sum_{\langle ij \rangle} \cos(\vartheta_i - \vartheta_j)\,. \tag{3.2}$$

The Lenz-Ising model has $\mathcal{Z}_2$ symmetry with spins allowed to take two discrete values $S_i = \pm 1$ at each lattice site i. In contrast, the XY model deals with continuous two component spins $(S_i^x, S_i^y) = (\cos\vartheta_i, \sin\vartheta_i)$ allowed to take any value on a ring of radius 1. The corresponding global symmetry is $O(2)$. In both cases only nearest neighbor interactions are considered, such that the summation in the Hamiltonian runs over all distinct nearest neigbor pairs $\langle ij \rangle$ only.

If the exchange constant fulfills the condition $J > 0$, the ground state at $T = 0$ K is a broken symmetry state where all spins point in one particular direction. One may now ask whether such a (long-range ordered) ground state is stable with respect to thermal fluctuations. On a heuristic level this question can most easily be answered with a scaling argument which

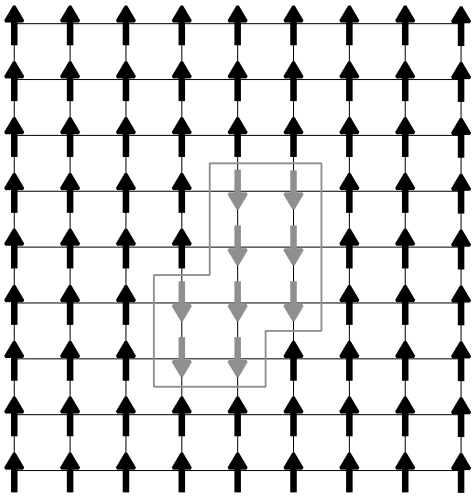

Figure 3.2: A droplet (island) of minority spins (grey) in a sea of a spin states favored by a magnetic field applied only at the boundaries of the 2d system.

goes back to Peierls (1935) and Landau (1937). Suppose that a magnetic field is applied only at the boundaries of a 2d system such as to energetically favor a particular spin orientation; see Fig. 3.2. To find out whether the system is stable against thermal fluctuations we ask for the free energy cost to create a droplet (island) of size l with an opposite spin orientation. The entropy gain is simply estimated by the number of configurations of a closed random walk, which scales as $Z_{\text{conf}} \sim z^l$, where z counts the number of ways to change direction at each step of the random walk (for a square lattice, $z < 3$). Thus, quite independent of the symmetry of the spin model, the *entropy gain* for the droplet scales as $S \sim k_B\, l\, \ln z$. The energy cost, in contrast, strongly depends on the symmetry. For the Lenz-Ising model there has to be a discrete spin flip at each site along the boundary of the island, such that the *energy cost* is $E \sim Jl$. This gives for the total free energy

$$F \sim Jl - k_B T l \ln z\,, \tag{3.3}$$

which implies that for sufficiently low temperatures the ferromagnetically ordered state should be stable. Quite generically one finds for models with discrete symmetry that a phase transition occurs at a temperature $T_c \sim O(J)$, which scales as the exchange energy J. The energy cost for a domain wall in the XY model is considerably lower since the spins are allowed to continuously change from the majority direction to the minority direction on the island. For the estimate we expand the Hamiltonian in Eq. 3.2 to harmonic order in the phases ϑ_i and take the continuum limit to find

$$\mathcal{H} = \frac{1}{2}\rho_s \int d^2 r (\nabla\vartheta(\mathbf{r}))^2\,, \tag{3.4}$$

where $\rho_s \sim J$ is a stiffness parameter for the phase fluctuations. Power counting then gives an energy cost which is independent of the size of the droplet, in contrast to the entropy which

still scales as l. Thus entropy always wins, such that a ferromagnetically ordered state is unstable against the proliferation of droplets. These observations are put on a rigorous basis by the Mermin-Wagner theorem (Mermin and Wagner 1966) stating that there is no long-range order in a two-dimensional system with short-range interaction and a continuous symmetry group. But even in systems with continuous symmetry, order is not destroyed alltogether. As has been shown by Wegner (1967) for the 2d XY model and by Jancovici (1967) for 2d solids there is still a low-temperature phase with QLRO, characterized by a power law decay of the order parameter correlation function. This phase is thermodynamically distinct from a high temperature phase with short-range order where correlation functions decay exponentially at large distances. A remarkable finding is that the excitations driving the transition are not long-wavelength fluctuations in the phase of the order parameter but topological defects, which drive the phase transition (Kosterlitz and Thouless 1972; Kosterlitz and Thouless 1973). Building on these ideas a defect mediated melting theory has been formulated with the remarkable result that melting of 2d solids proceeds via a successive unbinding of dislocations and disclinations with a *hexatic phase* intervening between the solid and the liquid phase (Halperin and Nelson 1978; Nelson and Halperin 1979).

3.2.1 Discrete symmetries

Lenz-Ising model

The Lenz-Ising model described by the Hamiltonian Eq. 3.1 was originally proposed as a crude model for ferromagnetism. By now it has become one of the pillars of statistical mechanics and is discussed at length in many textbooks; see e.g. the book by Huang (1987). Its simplicity arises due to the discrete $\mathcal{Z}_2$-symmetry of the Hamiltonian, i.e., its invariance under spin flips $S_i \to -S_i$. This symmetry is said to be spontaneously broken and the system becomes ferromagnetically ordered, when one spin state is thermodynamically favored at low temperatures (in the absence of an external magnetic field). The degree of order is measured by the average magnetization, $m = \langle S_i \rangle$. One of the milestones in statistical mechanics is the exact solution of the 2d Lenz-Ising model by Onsager (1944). His solution proves the existence of a ferromagnetic transition at a critical temperature $k_B T_c \approx 2.27J$, and gives a detailed characterization of its thermodynamics close to the transition point. For example, the magnetization is found to increase as $m \propto (T_c - T)^{1/8}$ in the ferromagnetic phase.

The Lenz-Ising model has a broad range of applications. Essentially it describes any interacting two-state model. In particular, there are mappings between spin order and lattice gas models, such as the order-disorder transitions in binary systems. Consider a 2d cubic lattice where each lattice site may be occupied by one atom of type A or B indicated by full and open symbols in Fig. 3.3. In order to write down the Hamiltonian describing the interaction between the A and B atoms one assigns spin variables

$$S_i = +1 \quad \text{if site } i \text{ is occupied by an A atom}\,, \tag{3.5}$$

$$S_i = -1 \quad \text{if site } i \text{ is occupied by an B atom}\,, \tag{3.6}$$

such that the occupation numbers become of the form

$$n_i^{A/B} = \frac{1}{2}(1 \pm S_i)\,. \tag{3.7}$$

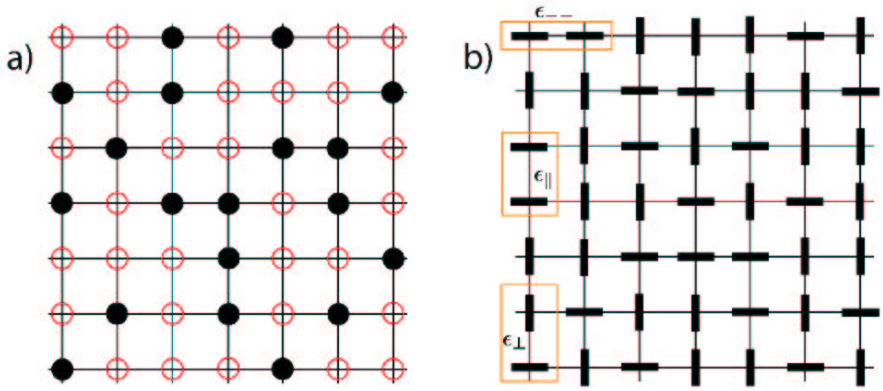

Figure 3.3: (a) Illustration of a binary system with A and B particles on a cubic lattice. A and B particles are indicated by full and open symbols. (b) Illustration for a lattice gas model, where rod-like molecules with two possible orientations occupy a square lattice. The rods can be oriented either vertically or horizontally, $S_i = \pm 1$. Nearest neighbor interaction depend on both the relative orientation of the rod-like particles and the orientation of the bond.

Then, with interaction energies $\epsilon_{\alpha\beta}$ between atoms of type $\alpha, \beta \in \{A, B\}$, the interaction energy for each bond $\langle ij \rangle$ reads

$$h_{ij}(S_i, S_j) = \epsilon_{AA} n_i^A n_j^A + \epsilon_{AB}(n_i^A n_j^B + n_i^B n_j^A) + \epsilon_{BB} n_i^B n_j^B \,. \tag{3.8}$$

This can easily be verified by explicitly inspecting all possible nearest neighbor configurations on the cubic lattice. The key observation is that the interaction energy can - up to a spin independent constant - also be written as

$$h_{ij} = -J S_i S_j \tag{3.9}$$

with $J = \frac{1}{4}(\epsilon_{AA} + \epsilon_{BB} - 2\epsilon_{AB})$ such that the lattice gas model is fully equivalent to a nearest-neigbour Lenz-Ising model. The only difference is that in a lattice gas there is a constraint $\sum_i S_i = 0$ since we assume the number of A and B atoms are equal; this may be accounted for by an appropriate Langrange multiplier.

A similar reasoning applies when studying more complex molecular crystals on patterned surfaces of different symmetry. The main idea is always to find an appropriate “spin language” for the possible states of the molecules at each lattice site and then to derive the corresponding Hamiltonian by considering all possible nearest-neighbor configurations. As a simple and illustrative example consider a generalization of the foregoing model, where each lattice site is occupied by a rod-like particles (“dimer”) with two possible orientations, either vertical or horizontal, signified again by a spin variable $S_i = \pm 1$, respectively (Vollmayr 1992); see Fig. 3.3 b.

Then, in general, the interaction energy h_{ij} between two neighboring sites will not only depend on the relative orientation of the rods but also on the orientation $\alpha = \pm 1$ of the bond connecting those lattices sites, such that we have $h_{ij}(S_i, S_j; \alpha)$. If both rods are in orientation

$S_i = +1$ (vertical) they are denoted by

$$h_{ij}(1,1;-1) = \epsilon_{\parallel} \,, \tag{3.10}$$
$$h_{ij}(1,1;1) = \epsilon_{--} \,. \tag{3.11}$$

The interaction energies of dimers in the horizontal direction ($S_i = -1$) also depend on the bond orientation, but because of the symmetry of the square lattice they are the same energies as before just in opposite order

$$h_{ij}(-1,-1;-1) = \epsilon_{--} \,, \tag{3.12}$$
$$h_{ij}(-1,-1;1) = \epsilon_{\parallel} \,. \tag{3.13}$$

The same symmetry also implies that the interaction energy of two perpendicular dimer orientations does not depend on the bond orientation

$$h_{ij}(1,-1;\pm 1) = h_{ij}(-1,1;\pm 1) = \epsilon_{\perp} \,. \tag{3.14}$$

In exactly the same way as for the binary system we may now write the interaction energy in terms of the spin variables. Since the only difference between the two bond orientations is that the energies $\epsilon_{\parallel}$ and ϵ_{--} are interchanged, we get for both bond orientations α

$$h_{ij}(S_i, S_j; \alpha) = J S_i S_j \,, \tag{3.15}$$

with $J = \frac{1}{4}(\epsilon_{\parallel} + \epsilon_{--} - 2\epsilon_{\perp})$, again up to a spin and bond orientation independent term. Though at first sight it appeared that this dimer model might be different from the Lenz-Ising model we finally arrived at the same Hamiltonian. This is, of course, not true in general. In later sections we will encounter examples of colloidal molecular crystals, where more general models emerge such as the Potts model to be discussed next.

Potts model

Upon generalizing the two-state Lenz-Ising model to $\sigma_i = 1, .., q$ equivalent states one arrives at the Hamiltonian for the q-state Potts model

$$\mathcal{H} = -J \sum_{\langle ij \rangle} \delta_{\sigma_i, \sigma_j} \,. \tag{3.16}$$

Here the only energetic contribution occurs if two neighboring spins are in the same state, $\sigma_i = \sigma_j$.

There have been intensive studies of the critical properties of ferromagnetic as well as antiferromagnetic Potts models for various lattice geometries in two and three dimensions. In particular, a rigorous solution of the ferromagnetic Potts model in two dimensions is available (Baxter 1973; Wu 1982) for a square, triangular, and honeycomb lattice for $q = 2$ (Lenz-Ising) and $q \geq 4$. The melting of the ferromagnetic phase to the paramagnetic one occurs via a continuous phase transition for the case of $q = 2, 4$ and via a discontinuous one for $q > 4$. For both cases the exact value of the critical temperature for the triangular lattice is given by

$$\exp(J/k_B T_c) = \begin{cases} 2\cos\left(\frac{2}{3}\cos^{-1}(\frac{\sqrt{q}}{2})\right) & \text{for} \quad q = 2, 4 \\ 2\cosh\left(\frac{2}{3}\cosh^{-1}(\frac{\sqrt{q}}{2})\right) & \text{for} \quad q \geq 4 \end{cases} \,. \tag{3.17}$$

For the interesting case of $q = 3$ (see section 3.4.1) neither the method of transfer matrices (for the Lenz-Ising model) nor the circle theorem for the vertex model (for $q \geq 4$ Potts models) is applicable. Nevertheless, since the critical point in Eq. 3.17 agrees with the exact Lenz-Ising result, it is expected that it holds also for $q = 3$. There is also a strong numerical evidence by Monte Carlo simulations that the critical temperature is still given by Eq. 3.17. It is interesting to note that a standard mean-field (MF) analysis gives a qualitatively wrong result as far as the nature of the transition is concerned, i.e., a discontinuous scenario is predicted for $q \geq 3$. The value of the critical temperature is overestimated,

$$k_B T_{\text{MF}} = \frac{3J}{2\ln 2}, \tag{3.18}$$

with respect to the "exact" value $k_B T_c = J/\ln[2\cos(\pi/9)]$ by a factor of 1.3654 similar to the case of the 2d Lenz-Ising model.

3.2.2 Continuous symmetries

2d XY model

The effect of fluctuations on the ordering behavior of 2d systems with continuous symmetry is illustrated best with the XY model. We have already seen that at low temperatures the Hamiltonian to harmonic order takes the form

$$\beta\mathcal{H} = \frac{1}{2}\int d^2r\, K\,(\nabla\vartheta(\mathbf{r}))^2\,, \tag{3.19}$$

where the fluctuations in the phase ϑ (orientation of the spin) are controlled by the stiffness parameter $K = \beta\rho_s$. These phase fluctuations (spin waves) are Goldstone modes with the tendency to decrease or even destroy long-range order. Indeed, one finds for the order parameter

$$\langle\cos\vartheta\rangle = \exp\left[-\frac{1}{2}\langle\vartheta^2(\mathbf{r})\rangle\right]\,, \tag{3.20}$$

where the local mean-square fluctuations (Debye-Waller factor)

$$W = \frac{1}{2}\langle\vartheta^2(\mathbf{r})\rangle = \frac{1}{2}\int\frac{d^2q}{(2\pi)^2}\,\frac{1}{Kq^2} \tag{3.21}$$

diverge logarithmically due to long wave length spin waves (which are only cut off by the system size). One concludes that there is no long range order for a 2d XY model. As in the scaling argument the reason is that there is little energy cost for the excitation of spin waves. These results are further corroborated by the Mermin-Wagner theorem which states that there can not be any spontaneous breaking of a continuous symmetry in $d \leq 2$ for systems with short-range interaction (Mermin and Wagner 1966).

Although there is no long-range order, correlations at low temperatures do not decay exponentially as in the paramagnetic phase but algebraically. One finds

$$\langle\mathbf{S}(\mathbf{r})\cdot\mathbf{S}(\mathbf{0})\rangle = \text{Re}\langle e^{i(\vartheta(\mathbf{r})-\vartheta(\mathbf{0}))}\rangle = e^{-\frac{1}{2}\langle[\vartheta(\mathbf{r})-\vartheta(\mathbf{0})]^2\rangle} \propto r^{-\eta(T)} \tag{3.22}$$

with a continuously varying temperature dependent exponent

$$\eta(T) = \frac{1}{2\pi K} \,. \tag{3.23}$$

This correlation function still approaches zero for large distances, which is consistent with the absence of long-range order. Such a phase is said to have *quasi-long-range order* (QLRO) . What makes this low temperature phase different from a high temperature phase is not only the slow power law decay of its correlations but also the finite value of the spin wave stiffness K.

Since it is known from high temperature series expansions that correlations have to decay exponentially if temperatures are large enough, these results also suggest that there is a phase transition at some critical temperature, where even QLRO must be lost. In order to describe this transition one has to go beyond the harmonic order, which obviously misses the fact that the phase ϑ is a periodic variable which is defined modulo 2π. As a consequence there are not only spin waves but also vortices as low lying excitations. In a vortex configuration, illustrated in Fig. 3.4, the phase varies little between neighboring spins but changes by a full period of 2π when followed around a large closed curve, $\oint d\vartheta = 2\pi$. In contrast to spin waves these excitations are topological defects which can not be made to disappear by any continuous deformation of the order parameter field. Let L be the system size. Then, such vortex configuration cost an energy which scales as $E \sim K \ln L$, but give a gain in entropy proportional to the logarithm in the number of lattice sites, $S \sim \ln L^2$. Balancing energy and entropy as in the Peierls argument then predicts a critical temperature $T \propto K$ above which isolated vortices may proliferate in the system; this argument is known as the Kosterlitz-Thouless criterion (Kosterlitz and Thouless 1972; Kosterlitz and Thouless 1973). Below the proliferation temperature vortices are bound and interacting logarithmically on long length scales (José et al. 1977). There is much more to say about the precise nature of the transition, which the reader may find in textbooks of Chaikin and Lubensky (1995) and Nelson (2002).

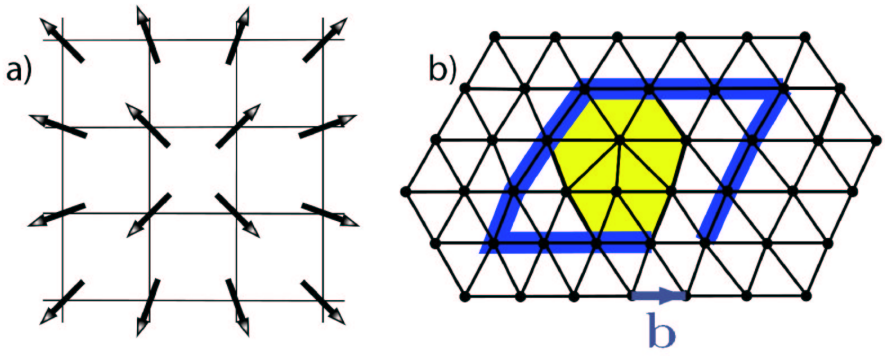

Figure 3.4: Illustration of topological defects. (a) Vortex configuration of spins in a two-dimensional XY model on a square lattice with charge $+1$. (b) Displacement field of a dislocation with Burgers vector $\mathbf{b}$ on a triangular lattice.

Melting of 2d solids

Similar physics applies to the discussion of melting of 2d solids. In a continuum elastic description in terms of a displacement field $\mathbf{u}(\mathbf{r})$ the coarse-grained Hamiltonian (effective free energy) reads

$$\mathcal{H} = \frac{1}{2} \int d^2r \, \left[2\mu u_{ij}^2(\mathbf{r}) + \lambda u_{kk}^2(\mathbf{r}) \right] , \tag{3.24}$$

where the stiffness parameters μ and λ are called Lamé coefficients, and we have employed sum convention. Due to rotational invariance the elastic energy is a function of the symmetric strain tensor only

$$u_{ij} = \frac{1}{2} \left(\partial_i u_j + \partial_j u_i \right) \tag{3.25}$$

but independent of the antisymmetric part

$$\theta = \frac{1}{2} \left(\partial_x u_y - \partial_y u_x \right) . \tag{3.26}$$

One may now proceed similar as for the 2d XY model and calculate the expectation value and the correlation function of the order parameter field, which for broken translational order is conveniently defined as the local Fourier component of the number density at the reciprocal lattice vector $\mathbf{G}$,

$$\rho_{\mathbf{G}}(\mathbf{r}) = e^{i\mathbf{G}\cdot\mathbf{r}} . \tag{3.27}$$

Since the Hamiltonian is quadratic in the displacement fields, calculations are quite straightforward. One finds that there is no long-range order, $\langle \rho_{\mathbf{G}}(\mathbf{r}) \rangle = 0$, and correlation functions decay algebraically

$$\langle \rho_{\mathbf{G}}(\mathbf{r}) \rho^{\star}_{\mathbf{G}}(\mathbf{0}) \rangle \propto r^{-\overline{\eta}_{\mathbf{G}}(T)} \tag{3.28}$$

with an exponent

$$\overline{\eta}_{\mathbf{G}}(T) = \frac{\mathbf{G}^2}{4\pi} \frac{k_B T}{\mu} \frac{3\mu + \lambda}{\mathbf{G}^2 \mu (2\mu + \lambda)} \tag{3.29}$$

that depends on temperature, the elastic coefficients and the particular reciprocal lattice vector $\mathbf{G}$. The power-law decay in the correlation functions leads to power-law singularites in the static structure factor

$$S(\mathbf{q}) = \sum_{\mathbf{r}} e^{i\mathbf{q}\cdot\mathbf{r}} \langle e^{i\mathbf{q}\cdot[\mathbf{u}(\mathbf{r}) - \mathbf{u}(\mathbf{0})]} \rangle \sim \frac{1}{\mid \mathbf{q} - \mathbf{G} \mid^{2 - \overline{\eta}_{\mathbf{G}}(T)}} , \tag{3.30}$$

where $\mathbf{q}$ signifies the wave vector. Instead of Bragg peaks, which would characterize true long-range order, the structure factor diverges algebraically at small reciprocal lattice vectors and displays cusps at larger ones.

There are two different types of topological defects associated with the continuum elasticity theory of a solid: dislocations and disclinations. Dislocations can be generated by removing a half-row of particles from an otherwise perfect lattice; see Fig. 3.4. They are quite effective in destroying translational order but are less disruptive of orientational correlations. The topological charge characterizing a dislocation is its Burgers vector $\mathbf{b}$, defined as the

amount that a closed contour integral of the displacement field around a dislocation fails to close $\oint d\mathbf{u} = \mathbf{b}$. One of the most remarkable results of 2d melting theory is that unbinding of dislocation pairs drives a transition from a solid not directly into a liquid but to an intermediate *hexatic phase* (Nelson and Halperin 1979), where translational order is short-range but there is still QLRO. A second transition from a hexatic to a liquid phase occurs only at a higher temperature where dissociation of disclination pairs destroys orientational correlations.

3.3 Substrate potentials with one-dimensional periodicity

Most atomic substrate potentials have two-dimensional (2d) periodicity. Some are characterized by a uniaxial symmetry, but due to the atomistic nature of the systems there is no substrate with a pure one-dimensional (1d) periodicity. Such an idealized model system has first been realized by Chowdhury et al. (1985) using a soft matter system. In their studies they subjected strongly interacting colloidal particles, confined in two dimensions, to a 1d periodic potential provided by the standing wave pattern of two interfering laser beams; see also section 3.3.4. As compared to their atomic counterparts these soft matter systems are much more versatile. For example, they allow to tune the depth of the substrate potential by simply tuning the laser intensity. Exploiting this new control parameter intriguing new phenomena like light induced freezing (Chowdhury et al. 1985) and melting (Wei et al. 1998) emerge.

In this section we discuss the ordering phenomena in two-dimensional colloidal systems which arise in the presence of a one-dimensional periodic potential. We will start our analysis with reviewing the theoretical work on this subject which is then followed by a discussion of the experimental results. The basic questions to answer are: What is the nature of the melting transition, if not preempted (as it can always be) by a first-order transition? More generally, how is the standard phase diagram for 2d melting on a homogeneous substrate (which includes the 2d crystal, hexatic and liquid phases) modified by the periodic laser potential? Which of the phases survive the light field and what new ones emerge in its presence? The answers to these and many other questions, provided below, lead to results consistent with experimental observations, and have many testable consequences for possible future experiments.

3.3.1 Commensurability and reciprocal lattice

For future reference this section serves to define the lattice geometry and its commensurability with the external periodic potential. A perfectly ordered hexagonal two-dimensional crystal is illustrated in Fig. 3.5. Its lattice sites $\mathbf{r}_n = n_1\mathbf{e}_1 + n_2\mathbf{e}_2$, with $n_{1,2} \in \mathbb{Z}$ are spanned by a set of lattice vectors

$$\mathbf{e}_1 = a\hat{\mathbf{e}}_x \ , \quad \mathbf{e}_2 = \frac{a}{2}(\hat{\mathbf{e}}_x + \sqrt{3}\hat{\mathbf{e}}_y) \ , \quad \mathbf{e}_3 = \frac{a}{2}(\hat{\mathbf{e}}_x - \sqrt{3}\hat{\mathbf{e}}_y) \ , \tag{3.31}$$

or equivalently, in Fourier space, the lattice is characterized by a set of three fundamental reciprocal lattice vectors

$$\mathbf{G}_1 = \frac{2\pi}{a'}\hat{\mathbf{e}}_y \ , \quad \mathbf{G}_2 = \frac{\pi}{a'}(\sqrt{3}\hat{\mathbf{e}}_x - \hat{\mathbf{e}}_y) \ , \quad \mathbf{G}_3 = \frac{\pi}{a'}(\sqrt{3}\hat{\mathbf{e}}_x + \hat{\mathbf{e}}_y) \ , \tag{3.32}$$

with $a' = a\sqrt{3}/2$ and a the mean colloidal spacing related to the particle density ρ by $\rho = 2/\sqrt{3}a^2$. An applied one-dimensional periodic potential may be characterized by its

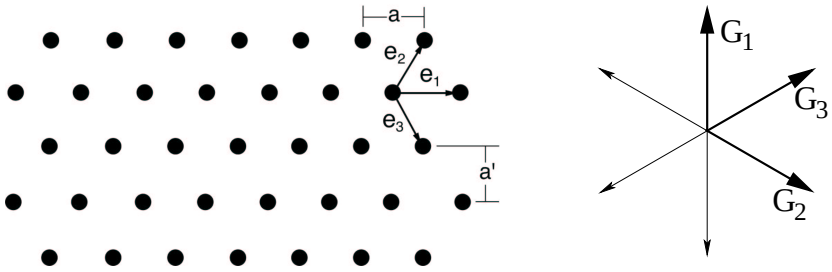

Figure 3.5: Illustration of a perfect hexagonal 2d crystal and the corresponding set of fundamental reciprocal lattice vectors.

energetically most important lowest harmonic $\mathbf{K}$, such that the part of the Hamiltonian containing the external potential reads for commensurable lattices

$$\mathcal{H}_{\mathbf{K}} = -V_0 \sum_n \cos\left(\mathbf{K}\cdot\left(\mathbf{r}_n + \mathbf{u}_n\right)\right) = -V_0 \int \frac{d^2r}{v} \cos(\mathbf{K}\cdot\mathbf{u}(\mathbf{r}))\,, \tag{3.33}$$

where $v = 1/\rho$ is the volume of the unit cell and $\mathbf{u}_n = \mathbf{u}(\mathbf{r}_n)$ denotes the displacement vector at site n; after the second equality sign a continuum limit has been performed. The coupling V_0 measures the strength of the $\mathbf{K}$th harmonic of the potential; see section 3.3.4 for a discussion of potentials created by interfering laser beams. For the purpose of the discussion in this section we have chosen an "internal" reference frame $(\hat{\mathbf{e}}_x, \hat{\mathbf{e}}_y)$ where the orientation of the hexagonal lattice is kept fixed. Later, beginning with subsection 3.3.2, we will switch to a "laboratory frame" $(\hat{\mathbf{x}}, \hat{\mathbf{y}})$ where the orientation of the laser potential is fixed with $\mathbf{K} = \frac{2\pi}{d}\hat{\mathbf{x}}$, i.e., the troughs are running parallel to the $\hat{\mathbf{y}}$-axis. Then the orientation of the lattice has to adjust correspondingly.
For a general wave vector $\mathbf{K}$, the periodic potential, characterized by a plane wave, $\exp(i\mathbf{K}\cdot\mathbf{r})$, will not be commensurate with the hexagonal lattice. Only for a particular orientation and magnitude of $\mathbf{K}$ the spacing between the potential minima will match with the periodicity of the hexagonal lattice. It is this special set of *commensurate* periodic potentials that is our focus here. The characteristic set of commensurate wave vectors is easy to find since the reciprocal lattice is *defined* to be the set of all wave vectors $\mathbf{G}$ that yield plane waves with the periodicity of a given Bravais lattice. Hence, commensurability is equivalent to the condition that $\mathbf{K}$ coincides with one of the reciprocal lattice vectors $\mathbf{G}$. In other words, the planes defined by the minima of the external potential are a superset of the family of lattice planes (Bragg planes) defined by the shortest reciprocal lattice vector, $\mathbf{G}_{\vec{m}} = m_1\mathbf{G}_1 + m_2\mathbf{G}_2$ with Miller indices m_1 and m_2, parallel to the wave vector of the external potential $\mathbf{K}$,

$$\mathbf{K} = p\mathbf{G}_{\vec{m}} = p_1\mathbf{G}_1 + p_2\mathbf{G}_2\ . \tag{3.34}$$

With $d = 2\pi/\mid\mathbf{K}\mid$ being the periodicity of the potential and $a'_{\vec{m}} = 2\pi/\mid\mathbf{G}_{\vec{m}}\mid$ defining the distance between the lattice planes, the *commensurability ratio* p is given by

$$p \equiv \frac{a'_{\vec{m}}}{d} = \frac{\mid\mathbf{K}\mid}{\mid\mathbf{G}_{\vec{m}}\mid}\ . \tag{3.35}$$

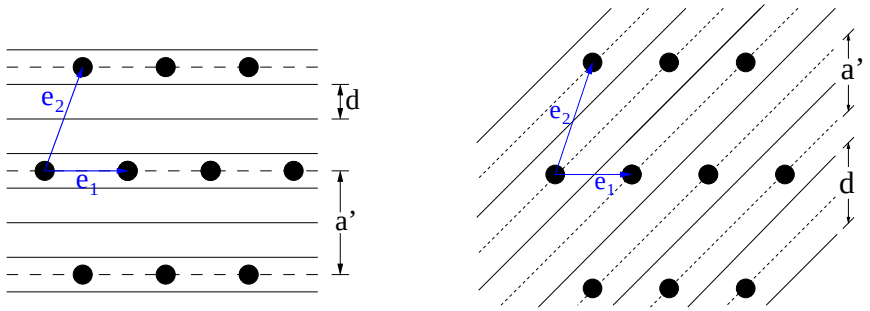

Figure 3.6: *Left:* 2d hexagonal colloidal crystal in the presence of a commensurate 1d periodic potential with period d, commensurability vector $\vec{p} = 3(1,0)$, and potential maxima indicated by solid lines. Dashed lines denote the Bragg rows picked out by the laser potential minima. *Right:* 2d hexagonal colloidal crystal in the presence of a commensurate 1d periodic potential with period d, commensurability vector $\vec{p} = (1,-1)$, and potential maxima indicated by solid lines. Dashed lines denote the Bragg rows picked out by the laser potential minima.

This allows us to characterize the laser potential by a set of Miller indices $\vec{m} = (m_1, m_2)$ and the commensurability ratio p, i.e., in summary, by a commensurability vector $\vec{p} = p\vec{m} = (p_1, p_2)$. Equivalently, the orientation of the Bragg planes can also be characterized by the shortest direct lattice vector pointing parallel to the troughs of the external potential,

$$\mathbf{R}_{\vec{n}} \equiv n_1\mathbf{e}_1 + n_2\mathbf{e}_2 \tag{3.36}$$

with the condition $\mathbf{R}_{\vec{n}} \cdot \mathbf{G}_{\vec{m}} = 0$, i.e., $(n_1, n_2) = (m_1, -m_2)$ a set of integers (direct lattice Miller indices), with no common factor complementary to the Miller indices.

On the left panel of Fig. 3.6 we have displayed an example for the simplest set of relative orientations between the periodic potential and the colloidal crystal. In our notation it corresponds to an orientation $(m_1, m_2) = (1,0)$ (or equivalently $(n_1, n_2) = (1,0)$) and a commensurability ratio $p = 3$, i.e., $\mathbf{K} = 3\mathbf{G}_{(1,0)} = 3\mathbf{G}_1$ and a Bragg row spacing $a'_{\vec{m}} = a' = a\sqrt{3}/2$. Because in such $\vec{m} = (1,0)$ orientations colloidal particles in neighboring Bragg planes are related by multiples of a *single fundamental* lattice vector, we call these relative orientations "primary". Note that in a reference frame, where the laser troughs are running parallel to the y-axis the configuration displayed on the left panel of Fig. 3.6 has to be rotated by $90°$.

In addition to these primary $\vec{p} = p(1,0)$ configurations, we will also discuss the next simplest $\vec{p} = p(1,-1)$ set of relative lattice–laser potential configurations, illustrated for $p = 1$ in the right panel of Fig. 3.6. These orientations are called "dual-primary", because they correspond to Bragg rows running perpendicular to a *fundamental real space* lattice vector with $\mathbf{K} = p(\mathbf{G}_1 - \mathbf{G}_2) = -\mathbf{e}_3 4\pi/a^2$, rather than to one of the three *fundamental reciprocal* lattice vectors. In terms of the direct lattice these dual-primary orientations correspond to $(n_1, n_2) = (1,1)$ and Bragg row spacing $a'_{\vec{m}} = a/2$.

3.3.2 Symmetry allowed phases and their description

What distinguishes a colloidal system subject to a 1d periodic potential from the corresponding system on a flat substrate is obviously its reduced symmetry. The 2d rotational symmetry is broken down to $\mathcal{Z}_2$ (Lenz-Ising) symmetry , corresponding to rotations by π. As one consequence all order parameters $\psi_n = e^{i2n\theta}$ are finite throughout the phase diagram and no sharp orientational ordering phase transition is possible. Furthermore, a coarse-grained description of any low temperature solid phase will in general have a uniaxial anisotropy such that the Hamiltonian contains four independent elastic constants (Frey et al. 1999; Radzihovsky et al. 2001)

$$\mathcal{H}_{\text{el}} = \int d^2r \left[2\mu u_{xy}^2 + \frac{1}{2}(\lambda_{xx}u_{xx}^2 + \lambda_{yy}u_{yy}^2) + \lambda_{xy}u_{xx}u_{yy} + 2(\alpha u_{xy}\theta + \gamma\theta^2) \right]. \tag{3.37}$$

In addition, for colloids on a patterned substrate, there are terms involving the anti-symmetric part of the strain tensor, $\theta = \frac{1}{2}(\partial_x u_y - \partial_y u_x)$. They describe the coupling between the local orientation of the lattice to the laser troughs (γ-term) but also to the strain field (α-term). Finally, the external potential (with potential troughs taken to run along the y–axis) also explicitly breaks continuous translational symmetry along x down to a discrete symmetry of translations by the period d of the potential. Hence all phases will trivially exhibit long-range order in the corresponding translational order parameter, leading to true delta-function Bragg peaks at the multiples of the reciprocal lattice vector $\mathbf{K} = (2\pi/d)\hat{\mathbf{x}}$ in their structure functions.

In the following we will discuss all phases allowed by symmetry starting with the most ordered, which naturally occurs at the lowest temperatures, and proceeding toward the higher temperature disordered phases, by invoking two types of disordering mechanisms, *dislocation unbinding* and *soliton proliferation*, discussed later in section 3.3.3.

Solid phases

As in the absence of a periodic potential, the most ordered phase of isotropic particles confined to 2d is a solid. The striking effect of turning on an external 1d periodic potential is that it can lead to two thermodynamically distinct uniaxially distorted hexagonal crystal phases, which have been termed *locked floating solid* (LFS) and *floating solid* (FS) (Frey et al. 1999; Radzihovsky et al. 2001). Being crystalline, both of these phases exhibit 2d translational (quasi-long-range) order, and are characterized by a finite shear modulus. These emerge as a result of breaking the translational symmetry $T_d^x \otimes T^y$ of the "modulated liquid" (ML) (see below), corresponding to independent discrete translations by $d\hat{\mathbf{x}}$ and continuous translations along $\hat{\mathbf{y}}$, down to 2d discrete translations generated by lattice vectors $\mathbf{e}_1$ and $\mathbf{e}_2$, Eqs.3.31. Although in the presence of thermal fluctuations dislocations will be thermally nucleated, in the solid phases they are confined to finite size dipoles with a zero Burgers "charge". These, therefore, lead to only weak *finite* renormalization of the elastic constants, and a purely elastic description in terms of phonon modes u_x and u_y is appropriate in both phases.

The *floating solid* can be rigorously differentiated from its locked counterpart as a 2d colloidal crystal phase by its ability to slide (float) *across* the troughs of the periodic potential; technically, the periodic potential is irrelevant (in the renormalization group sense) and

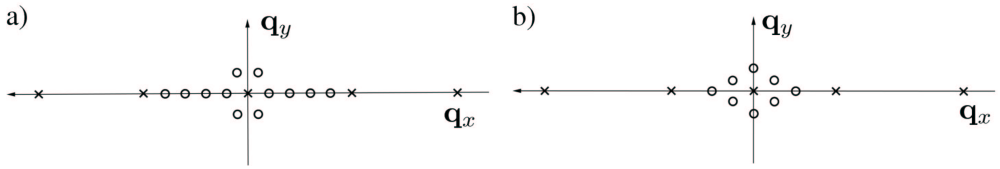

Figure 3.7: Schematic structure function for the FS phase with the commensurability vector (a) $\vec{p} = (0, 5)$ and (b) $\vec{p} = (-2, 2)$, illustrating a combination of the quasi- and true Bragg peaks, given by Eq. 3.38. Crosses indicate true Bragg peaks and open circles quasi-Bragg peaks.

therefore can be treated perturbatively. This implies that at long scales, many, but not all of the thermodynamic properties of the FS are well described by the elastic Hamiltonian $\mathcal{H}_{\rm el}$, Eq. 3.37, with two coupled *"massless"* u_x and u_y degrees of freedom, and ignoring $\mathcal{H}_{\mathbf{K}}$, 3.33. Therefore, in many ways the FS is qualitatively quite similar to a 2d solid without the periodic pinning potential. In particular, this similarity extends to the lattice displacement correlation functions which are logarithmic in x and y. However, these similarities do not extend to all correlation functions, and the periodic pinning potential has important qualitative consequences for the FS phase that distinguish it from an ordinary 2d solid. To illustrate this point, recall that the periodic potential *explicitly* breaks rotational and translational symmetry, despite its irrelevance in the FS phase. While the former leads to uniaxial anisotropy in the hexagonal lattice, the latter is responsible for the true long-range order in the translational order parameter $\rho_{\mathbf{G}}(\mathbf{r})$, with $\mathbf{G} = \pm n\mathbf{K}$ integer multiples of the wave vector $\mathbf{K}$. Other translational order parameters, with $\mathbf{G}$ *not* satisfying the above condition have pure power-law correlation functions, decaying to zero at long separations. This implies that the structure function shows true Bragg peaks (with power-law corrections) at multiples of the periodic potential wave vector $\mathbf{K}$ and pure power-law (quasi-) Bragg peaks at *all other* reciprocal lattice vectors $\mathbf{G}$, even for those with $\mathbf{G} \parallel \mathbf{K}$,

$$S(\mathbf{q}) \approx \sum_{\mathbf{G}} \frac{1}{|\mathbf{q} - \mathbf{G}|^{2-\overline{\eta}_{\mathbf{G}}}} + \sum_{n\neq 0} A_n \delta(\mathbf{q} - n\mathbf{K}) \ , \tag{3.38}$$

with $A_n \sim V_0^{2n}$. A schematic illustration of $S(\mathbf{q})$ for a floating solid is shown in Fig. 3.7 for the commensurability vectors $\vec{p} = (0, 5)$ and $\vec{p} = (-2, 2)$, respectively, with the x-axis chosen to point along $\mathbf{K}$. The set of on-$\hat{\mathbf{q}}_x$-axis quasi-Bragg peaks (indicated by open circles) interleaving the true Bragg peaks (indicated by "$\times$") is the notable feature that distinguishes the FS from its locked counterpart LFS, in which all on-$\hat{\mathbf{q}}_x$-axis peaks are true Bragg peaks.

At sufficiently low temperatures, the periodic potential will always be a relevant perturbation, pinning the 2d solid in the direction perpendicular to its troughs. Because of the 1d nature of the pinning potential, the 2d crystal will remain unpinned along the direction of the potential minima and will still be able to adjust freely in that direction. Hence, unlike the FS phase, the LFS is characterized at long wave lengths by one acoustic (u_y) and one optical (u_x) phonon mode, with an effective Hamiltonian for the *locked floating solid*. The corresponding Hamiltonian reads

$$\mathcal{H}_{\rm LFS} = \frac{1}{2} \int d^2r \left[B_{xy} (\partial_x u_y)^2 + B_{yy} (\partial_y u_y)^2 + \frac{\mu}{\xi^2} u_x^2 \right] \ , \tag{3.39}$$

where $B_{xy} = \mu + \gamma - \alpha$ and $B_{yy} = \lambda_{yy}$ are effective elastic constants and ξ is a correlation length that depends on the relative strength of the laser intensity to the elastic energy (Radzihovsky et al. 2001). Hence the fluctuations parallel to the troughs still exhibit a logarithmic divergence, and the connected part of the correlation function has the form

$$C_{\mathbf{G}}^{(c)}(\mathbf{r}) \sim r^{-\eta_{G_y}} \,, \tag{3.40}$$

where

$$\eta_{G_y} = \frac{G_y^2}{2\pi} \frac{k_B T}{\sqrt{B_{yy} B_{xy}}} \approx \frac{G_y^2}{2\pi} \frac{k_B T}{\sqrt{\mu(2\mu + \lambda)}} \,. \tag{3.41}$$

Here, the approximate expression holds if the effect of the periodic potential on elasticity and renormalizations due to dislocation pairs on the effective elastic coefficients is neglected. A discrete Fourier transform of this correlation function gives the corresponding structure function

$$S(\mathbf{q}) \approx \sum_{\mathbf{G}} \left[\frac{B_G}{|\mathbf{q} - \mathbf{G}|^{2-\eta_{G_y}}} + A_G \delta(\mathbf{q} - \mathbf{G}) \right] \,, \tag{3.42}$$

where the amplitudes are given by $B_G \propto \xi^{-\overline{\eta}_{G_x}}$ and $A_G \propto \delta_{G_y,0}\, \xi^{-\overline{\eta}_{\mathbf{G}}}$, which is finite *if and only if* $\mathbf{G}$ is parallel to $\mathbf{K}$; in addition the amplitude A_G will also have a background analytic part in V_0, which in a weak pinning limit scales as V_0^2, and therefore at higher temperatures will dominate over the nonanalytical part. As noted above, schematically the structure function $S(\mathbf{q})$ looks similar to Fig. 3.7 with the modification that now all peaks on the $\hat{\mathbf{q}}_x$–axis are real Bragg peaks. These results for the structure function of the LFS, displaying amplitudes that vanish as nontrivial powers of the periodic potential strength explain corresponding experimental observations of Chowdhury et al. (1985).

Smectic phases

As was first pointed out by Ostlund and Halperin (Ostlund and Halperin 1981), in uniaxial two-dimensional lattices, dislocations with Burgers vector along and perpendicular to the uniaxial axis will generically have different core energies and will therefore proliferate at different temperatures. This will consequently allow the possibility of a phase that is intermediate between a fully ordered crystal and a completely disordered liquid. In a commensurate orientation, such that Bragg rows coincide with the periodic potential troughs, dislocation pairs with Burgers vectors parallel to the potential minima are expected to unbind first. The resulting class of thermodynamically distinct phases are smectics. Their main common characteristic is that they display a finite elastic modulus for shear deformations perpendicular to the Burgers vector of unbound dislocations, but do not resist shear parallel to them, possessing only liquid-like correlations between the corresponding "atomic" rows. Consequently, such 2d smectics display 1d periodicity perpendicular to the Burgers vector of unbound dislocations; see Fig. 3.8

These smectics formed on a 1d periodic substrate are fundamentally distinct from the smectic phases found in liquid crystal materials and substrate-free smectics as discussed by

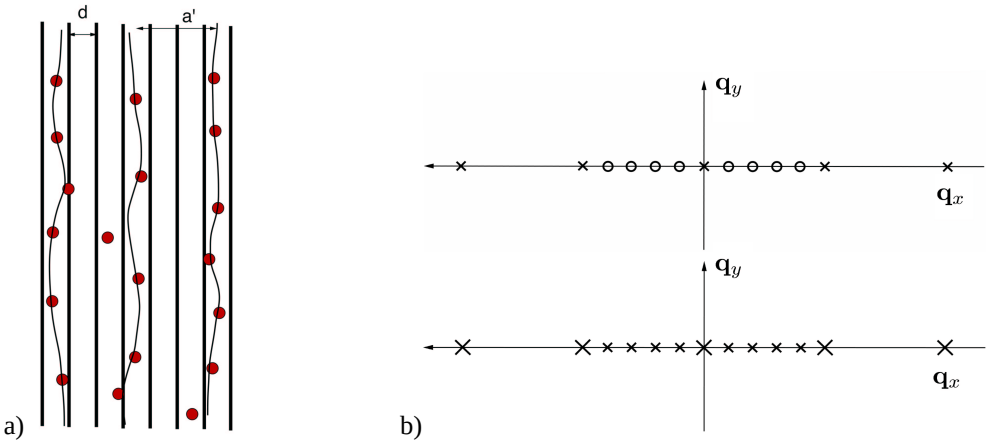

Figure 3.8: (a) Illustration of a 2d colloidal smectic phase in the presence of a commensurate 1d periodic potential with period d, commensurability parameter $p = 3$, and potential maxima indicated by full vertical lines. Thin lines denote the maxima in the smectic density, which are pinned inside the minima of the periodic laser potential. (b) *top:* Schematic of the structure function for the floating smectic phase, characterized by on-$\hat{\mathbf{q}}_x$-axis quasi-Bragg peaks (open circles) and true Bragg peaks (crosses). *bottom:* Schematic of the structure function for the locked smectic phase, characterized by on-$\hat{\mathbf{q}}_x$-axis true Bragg peaks, with small and large crosses indicating spontaneously and directly induced translational order.

Ostlund and Halperin (1981). The most important distinction is that in liquid crystal smectics and those without an underlying pinning substrate, the orientational symmetry is broken *spontaneously* leading to a soft Laplacian-curvature (rather than gradient-tension) elasticity, which preserves this underlying symmetry even in the smectic phase, where it is nonlinearly realized (de Gennes 1974; Chaikin and Lubensky 1995). In fact such substrate-free 2d smectics, because of the softness of their elasticity, are well known to be unstable to thermally-driven unbinding of dislocations, and at length scales longer than the distance between these free dislocations are therefore indistinguishable from a nematically-ordered 2d liquid (Toner and Nelson 1981). Such thermal instability of substrate-free 2d lattices precludes the existence of thermodynamically distinct intermediate 2d smectic phase in which only one set of Burgers vectors (e.g., along the uniaxial direction) unbind (Ostlund and Halperin 1981). However, in strong contrast to those rotationally invariant systems, in 2d lattices discussed here the periodic (laser) potential *explicitly* breaks rotational symmetry. As a consequence dislocation pairs with Burgers vector having components *along* $\mathbf{K}$ are bound by a linear potential. Since such dislocations remain bound even when those with Burgers vectors *perpendicular* to $\mathbf{K}$ unbind, they allow the existence of 2d smectic phases that are thermodynamically distinct from a liquid.

In close analogy to the translational order parameter of the 2d crystal, the smectic is distinguished from a liquid by a finite translational order parameter $\rho_{\mathbf{G}} = e^{i\mathbf{G}\cdot\mathbf{u}}$, but with a *single* (rather than a set, Eq. 3.32) reciprocal vector $\mathbf{G} = G\hat{\mathbf{x}} = (2\pi/a)\hat{\mathbf{x}}$. It is related to the total molecular density via a standard relation (de Gennes 1974)

$$\rho_{SM}(\mathbf{r}) = \mathrm{Re}[\rho_0 + e^{iGx}\rho_{\mathbf{G}}(\mathbf{r})] \ , \tag{3.43}$$

where ρ_0 is the mean density of the smectic. Of course, in the presence of a 1d periodic potential, a smectic is a thermodynamically distinct phase only if $\mathbf{G} = (2\pi/a)\hat{\mathbf{x}}$ differs from the wavevector $\mathbf{K}$ characterizing the external potential and the modulated liquid. Commensurate smectics are equivalently characterized by the ratio of their period a to that of the periodic potential d, with commensurability ratio $a/d \equiv p \in \mathbb{Z}$. A p-smectic then spontaneously breaks the discrete translational symmetry $T_d^x \otimes T^y$ of the modulated liquid, with its equal occupancy of each potential minima down to $T_a^x \otimes T^y$, with only every pth minima equivalently populated. Clearly then $p = 1$ is indistinguishable from the fully disordered modulated liquid.

The above symmetry considerations uniquely specify the Hamiltonian that characterizes the p-smectic phase

$$\mathcal{H}_{\rm Sm} = \int d^2r \left[\frac{1}{2}\Big(B_{yx}(\partial_y u_x)^2 + B_{xx}(\partial_x u_x)^2 \Big) - \frac{1}{v} V_0 \cos\big(K u_x(\mathbf{r})\big) \right] , \tag{3.44}$$

which is an anisotropic scalar Sine-Gordon model in the phonon field $u_x(\mathbf{r})$. Given the form of the Hamiltonian in Eq. 3.44, there is a close similarity between the properties of the smectic and the 2d crystal, studied in the previous section. The quantitative differences between these phases are due to the distinction between the vector ($\mathbf{u}$) and scalar (u_x) nature of elastic degrees of freedom in the 2d solid and smectic, respectively. More specifically, in close analogy to the 2d solid, it was found that for a fixed integer commensurability ratio p, there exist a low temperature locked and higher temperature floating smectic phase (Frey et al. 1999; Radzihovsky et al. 2001). These are distinguished by the importance of the periodic pinning potential.

In the *floating smectic phase (FSm)*, thermal fluctuations in the position of the layers are sufficiently large that at long length scales they average away many effects of the periodic pinning potential. Hence, many of the static properties of the FSm phase can be well described by the Hamiltonian, Eq. 3.44, with $V_0 = 0$. However, as noted in the discussion of the FS phase, despite of the renormalization group (RG) irrelevance of the periodic potential, continuous translational symmetry is still explicitly broken by it, which leads to true long-range translational order in the smectic order parameter $\rho_{\mathbf{G}}$ for $G\hat{\mathbf{x}}$ at multiples of the reciprocal lattice vector $K\hat{\mathbf{x}}$, characterizing the laser potential. The connected part of the correlation function again shows a power-law form

$$C_{\mathbf{G}}^{(c)}(\mathbf{r}) \sim r^{-\eta_{\rm FSm}} , \tag{3.45}$$

with the exponent

$$\eta_{\rm FSm} = \frac{k_B T G^2}{2\pi\sqrt{B_{yx}B_{xx}}} . \tag{3.46}$$

The disconnected part of the smectic translational correlation function is finite only at $G = nK$ ($n \in \mathbb{Z}$). The corresponding floating smectic structure function is given by an expression similar to the FS, Eq. 3.38. The only difference is that $\overline{\eta}_{\mathbf{G}}$ of the FS is replaced by $\eta_{\rm FSm}$ of the FSm and the summation over G is a sum over integer multiples of $2\pi/a$. Consequently, one expects to see sharp peaks only on the $\hat{\mathbf{q}}_x$–axis, with power-law peaks at $G \neq nK$, and true Bragg peaks at $G = nK$. This FSm structure function is schematically displayed in Fig. 3.8 b.

As the temperature is lowered, the periodic potential becomes relevant, pinning the smectic layers. The resulting *locked smectic (LSm)* phase is characterized by long-range translational order, and, as illustrated in Fig. 3.8, displays true Bragg peaks at all values of the on-$\hat{\mathbf{q}}_x$–axis reciprocal lattice vectors $G = n2\pi/a$. At long scales, the effective elastic Hamiltonian that characterizes this phase is simply

$$\mathcal{H}_{\mathrm{LSm}} = \frac{1}{2}\frac{\mu}{\xi^2}\int d^2r\; u_x^2\;. \tag{3.47}$$

Modulated liquid (ML)

The modulated liquid is the most disordered phase, which occurs at highest temperatures and does not *spontaneously* break any symmetries. It is characterized by a vanishing shear modulus, unbound dislocations, absence of massless Goldstone modes, and a discrete symmetry of translations along the x-axis by periodic potential constant d. The corresponding structure function of this explicitly orientationally ordered phase is a set of true Bragg peaks at multiples of the reciprocal lattice vector $K = 2\pi/d$ of the periodic potential. *Finite linear* translational order parameter susceptibility guarantees that the average order parameter is linear in the strength of the periodic potential. Therefore, the strength of the Bragg peaks scales as a *cube* of the input laser intensity, proportional to V_0, as observed in experiments by Chowdhury et al. (1985).

3.3.3 Phase diagrams and phase transitions

The topology of the phase diagram strongly depends on the level of commensurability between the colloidal crystal and the laser potential. There are two important ingredients: (i) the orientation of the triangular colloidal lattice relative to that of the periodic potential troughs, which selects a set of Bragg planes that run parallel to the troughs, (ii) the commensurability ratio of the spacing a' between these Bragg planes to the period d of the laser potential, defined by $p \equiv a'/d$.

Starting from a locked floating solid at low temperatures there are several distinct melting scenarios (Frey et al. 1999), depending mainly on the magnitude of the commensurability ratio. For p smaller than some critical value p_c the locked floating solid melts by the unbinding of dislocations with Burgers vectors parallel to the direction of the laser troughs since only those dislocations have the usual logarithmically divergent energies. Dislocations with other directions of the Burgers vector are disfavored since they are attached to a semi-infinite discommensuration strings (Pokrovsky 1986). In Figs. 3.9a and b, two particularly interesting relative orientations of the colloidal crystal and laser potential are shown. For the orientation in Fig. 3.9a, four of the six fundamental Burgers vectors are disfavored by the potential. This is also reflected in the schematic illustration of the static structure factor. In the second orientation, Fig. 3.9 b, all *six* fundamental Burgers vectors are disfavored. The lowest energy Burgers vector parallel to the troughs has length $|\mathbf{b}| = \sqrt{3}a$. Since, as discussed below, dislocation mediated melting theory predicts a melting temperature proportional to the magnitude of the Burgers vector squared, the relative orientation of the colloidal lattice and the substrate potential will control the melting transition. For the present case this implies an increase by a factor

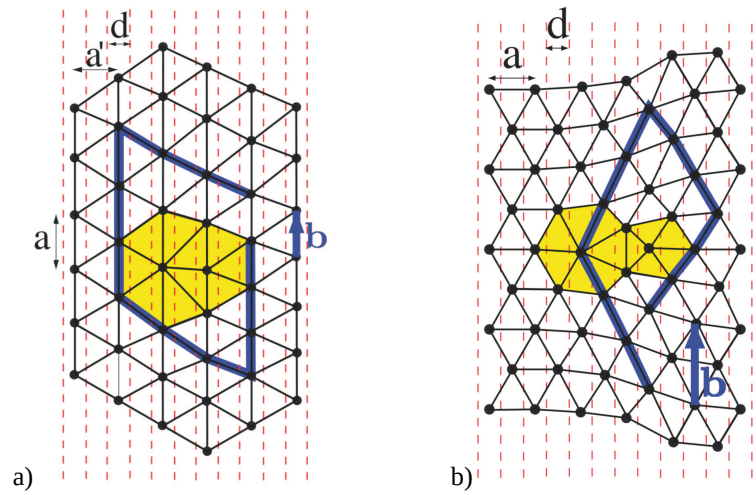

Figure 3.9: (a) Triangular lattice with lattice constant a subject to a periodic potential (maxima indicated by dashed lines) for $pd = a'$ with $a' = \sqrt{3}a/2$ and $p = 2$. Also shown is the low energy dislocation with Burgers vector $\mathbf{b}$ parallel to the corrugation of the external potential. (b) Triangular lattice with lattice constant a subject to a periodic potential (maxima indicated by dashed lines) for a dual-primary orientation with $pd = a'$, where $a' = a/2$ is the Bragg plane spacing and the commensurability ratio is $p = 1$. Also shown is the low energy dislocation with Burgers vector $\mathbf{b}$ parallel to the corrugation of the potential.

of 3. This is consistent with experimental data (Bechinger et al. 2000) which suggest that the onset of light induced freezing at *fixed temperature* is shifted to smaller laser intensities also by roughly a factor of 3 when the trough spacing is changed between $d = 8 - 4\,\mu$m.

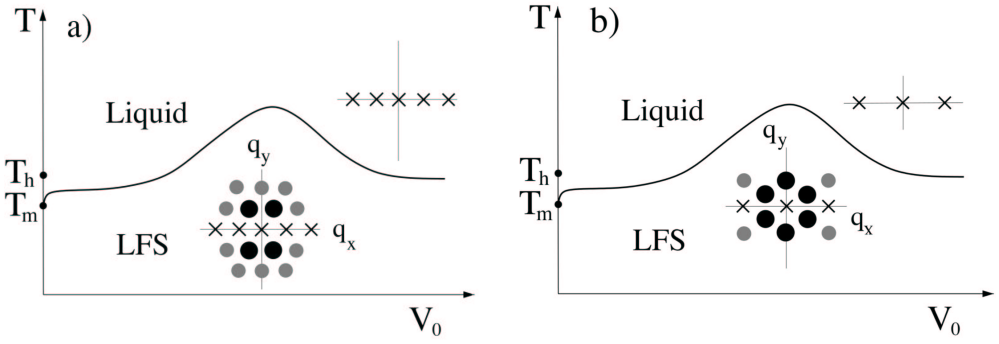

Figure 3.10: Schematic phase diagram for a primary commensurate orientation with commensurability parameter $p = 1$, but two different relative orientations of the colloidal lattice and the substrate potential, as illustrated in Fig. 3.9. Both the magnitude of the melting temperature and the behavior of the static structure factor are controlled by the relative orientation. *Insets:* Schematic static structure factors in the various phases. The $\times$'s indicate delta-function Bragg peaks and the shaded circles algebraic peaks.

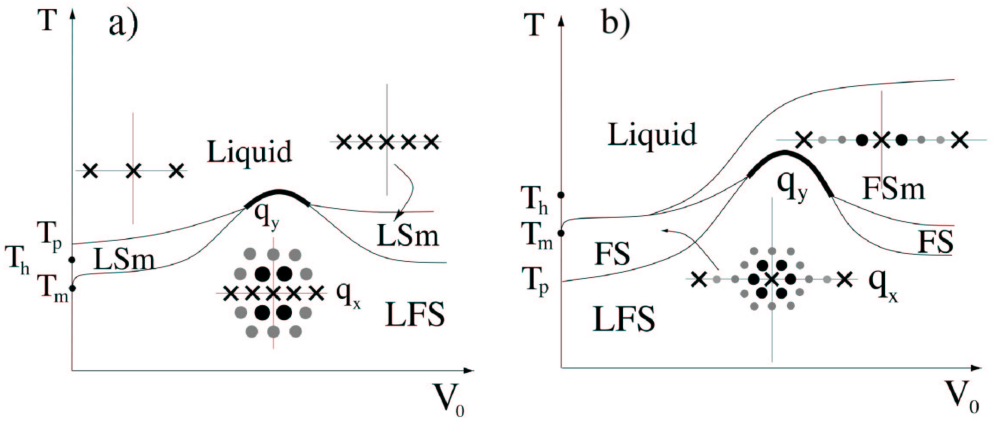

Figure 3.11: Schematic phase diagram for a primary commensurate orientation with commensurability parameters: a) $2 \leq p \leq p_c$ and b) $p \geq p_c$ (the case $p = 4$ is shown here). Thick line indicates a first order transition. *Insets:* Schematic structure functions in the various phases. The $\times$'s indicate delta-function Bragg peaks and the shaded circles algebraic peaks.

Because the sharp distinction between the hexatic and isotropic liquid phase is absent in the presence of a periodic potential, the phase diagram for $p = 1$ contains only two thermodynamically distinct phases at finite V_0: the modulated liquid and a locked floating solid (LFS). The most striking feature of the melting transition is the shape of the phase boundary $T_{\rm m}(V_0)$, whose universal features guarantee a generically reentrant melting, under typical experimental conditions (Wei et al. 1998). We will come back to this issue later in section 3.3.6.

The nature of the ensuing phase after dislocation pair unbinding depends on the value of p. Whereas for $p = 1$ it is a modulated liquid, symmetry also allows for an intervening locked smectic phase for $p \geq 1$; compare Figs. 3.10 and 3.11 for an illustration of the different phase diagram topologies. As discussed in the previous section, the LSm phase distinguishes itself from the modulated liquid by spontaneously breaking the liquid's discrete translation symmetry by d down to translations by $p \times d$. In contrast to the LFS, however, the LSm exhibits only short-range correlations between colloidal positions lying in different troughs. Symmetry dictates that the melting of the LSm into the modulated liquid phase is in the p-state clock model universality class. In contrast, the LFS melts into the LSm through a transition in the XY universality class and will therefore also exhibit the usual Kosterlitz-Thouless phenomenology (Kosterlitz and Thouless 1973). The phase diagram also includes the possibility of a direct transition from the LFS to the modulated liquid at intermediate potential strength. This transition is expected to be different than the LFS-liquid transition for $p = 1$. Whereas the $p = 1$ transition is in the XY universality class, for $1 < p < p_c$ the LFS-liquid transition is associated with simultaneous loss of XY and discrete (Lenz-Ising for $p = 2$) order. Because at this latter transition two unrelated symmetries are simultaneously restored, it is expected to be first order (Frey et al. 1999; Radzihovsky et al. 2001). At the multicritical point, where the liquid, LFS and LSm phases meet, the critical behavior is presumably described by a two-dimensional compressible p-state clock model (Bergman and Halperin 1976).

For large commensurability ratios, the complexity of the 2d colloidal phase diagram (displayed in Fig. 3.11 b) further increases, allowing also floating phases, the "floating solid" (FS) and the "floating smectic" (FSm). Let us reemphasize that the floating phases are distinguished from their "locked" counter parts, the LFS and LSm, by their ability to slide (float) *across* the troughs of the periodic potential; technically, the periodic potential is irrelevant (in the renormalization group sense) and therefore can be treated perturbatively inside the FS and FSm phases. As illustrated in Fig. 3.11, all the *spontaneously* induced structure function peaks of these floating phases are *quasi*-Bragg peaks, and therefore the corresponding density correlation functions display real-space *power-law* decay. Although, in principle, the critical values $p_c^{\rm S}$, $p_c^{\rm Sm}$ for the appearance of each of these floating phases are most likely distinct, for simplicity of the presentation we have taken $p_c^{\rm S} = p_c^{\rm Sm} \equiv p_c$. If in reality these critical values are sufficiently distinct, and $p_c^{\rm S} < p_c^{\rm Sm}$, then one expects an intermediate range of p values, $p_c^{\rm S} < p < p_c^{\rm Sm}$, for which no FSm appears.

The phase transitions between the corresponding locked and floating phases (LFS-FS and LSm-FSm) are in the same universality class as the well-known thermal roughening transition, the dual of the Kosterlitz-Thouless transition (José et al. 1977), with an identical phenomenology; see the discussion below. Similar to the XY-melting LFS-LSm transition discussed above, the melting of the FS into the FSm proceeds via unbinding of dislocation pairs with x-directed Burgers vectors. However, because of the presence of massless spectator phonon modes in y-direction (transverse to the troughs of the periodic potential), the melting of the FS into the FSm is in a new universality class (Frey et al. 1999; Radzihovsky et al. 2001).

The direct transition from the LFS to the FSm phase is most likely first order. Here the order of the u_y-modes changes from quasi-long-range to short-range (via unbinding of type I dislocations, i.e., those with Burgers vector parallel to the troughs of the periodic potential.) and for the u_x-modes from long-range to quasi-long-range (via depinning from the laser potential, i.e., a roughening transition). If both order parameters become critical at the same point in the phase diagram, which will be the case at the multicritical points where the FS, LFS, and FSm phases meet, we have a simultaneous phase transition of the Kosterlitz-Thouless type and its dual analog.

Roughening transitions

Phase transitions that fall into the roughening transition universality class separate a low temperature ordered phase, in which a potential Goldstone mode is strongly pinned by an external periodic potential, from a quasi-long-range ordered phase, in which the periodic potential is irrelevant in a renormalization group sense. The locked floating solid to floating solid and the locked smectic to floating smectic transitions, both fall into this broad universality class. The main lines of the analysis of these transitions are quite similar and can be done via standard perturbative momentum-shell RG transformation (José et al. 1977). Since the smooth (locked) and rough (floating) phases are distinguished by the relevance and irrelevance of the periodic potential, respectively, one can find the transition temperature by analyzing the behavior of the laser potential $\mathcal{H}_{\mathbf{K}}$ as a function of length scale. For the periodic pinning potential coupling

V_0, a standard renormalization group calculation (Radzihovsky et al. 2001) gives

$$V_0(\ell) = V_0 \exp\left[2\ell - \frac{1}{2}K_x^2\langle u_x^2\rangle_>\right] , \tag{3.48}$$

where $\langle u_x^2\rangle_>$ has to be computed with the elastic Hamiltonian appropriate to the phase being analyzed, keeping only modes q within a momentum shell $\Lambda e^{-\ell} < q < \Lambda$ near the zone boundary Λ. Hence the nature of the pinning by the substrate potential and the transition temperature obviously depend on the degree of translational order in the system, i.e., whether the phase is a solid or a smectic.

Upon using the explicit forms of the elastic Hamiltonians, Eq. 3.37 and Eq. 3.44, respectively, one finds that both grow linear in ℓ, such that $V_0(\ell) = V_0 \exp[\lambda_{\rm p}(T)\,\ell]$. The transition temperatures are then found by setting the eigenvalue $\lambda_{\rm p}(T_{\rm p}) = 0$. This results in a depinning temperature separating the LFS and the FS phase,

$$k_{\rm B}T_{\rm pS} = 8\pi\overline{\mu}\left(\frac{d}{2\pi}\right)^2 , \tag{3.49}$$

with $\overline{\mu} = 2\mu(2\mu+\lambda)/(3\mu+\lambda)$. Here, for simplicity, the result in the dilute limit has been given, where the Debye screening length is much smaller than the lattice spacing. The corresponding phase boundary from the LSm to the FSm reads

$$k_{\rm B}T_{\rm pSm} = 8\pi\sqrt{B_{xx}B_{yx}}\left(\frac{d}{2\pi}\right)^2 . \tag{3.50}$$

Dislocation unbinding transitions

In the analysis of the preceding section, where a thermal depinning transition within the solid phase was studied, it was implicitly assumed that the dislocations that distinguish the 2d solid and the smectic phases from the higher temperature disordered phases remain bound. Hence, these results remain valid only if they fall below the corresponding dislocation unbinding melting transition temperatures, which will be discussed now.

The most striking consequence of the 1d periodic potential is that it leads to the LFS phase, in which the phonon degree of freedom, u_x, corresponding to displacements transverse to the potential troughs are effectively suppressed. Therefore, this phonon mode can be safely integrated out, leaving an effective anisotropic 2d XY Hamiltonian, with temperature and potential strength dependent *effective* elastic constants ,

$$\mathcal{H}_{\rm LFS} = \frac{1}{2}\int d^2r\Big(B_{xy}(\partial_x u_y)^2 + B_{yy}(\partial_y u_y)^2\Big) . \tag{3.51}$$

Melting of the LFS can be understood in terms of dislocation unbinding. However, in contrast to melting in the absence of an external potential (Nelson and Halperin 1979) here only the so-called type–I dislocation pairs with Burgers vectors $\pm\mathbf{b}_1 = \pm b_{\vec{n}}\hat{\mathbf{y}}$ aligned parallel to the trough direction can be thermally unbound. In the presence of a periodic potential, oppositely charged dislocations, with Burgers vectors not satisfying the above condition (type–II dislocations) are bound by a potential which grows linearly with the separation and therefore cannot

thermally unbind. This discussion is consistent with the mapping onto *scalar* Coulomb gas Hamiltonian, expected to describe logarithmically bound type–I dislocations, embodied in the 2d anisotropic XY model Hamiltonian, Eq. 3.51. A standard calculation (Nelson and Halperin 1979) leads to the prediction for the LFS melting temperature (Frey et al. 1999; Radzihovsky et al. 2001)

$$k_{\rm B}T_{\rm LFS-LSm} = \frac{b_{\vec{n}}^2}{8\pi}\sqrt{B_{xy}B_{yy}}\ , \tag{3.52}$$

and all other concomitant Kosterlitz-Thouless phenomenology. The resulting high temperature phase is the LSm, for low colloidal densities (i.e., high commensurability ratio p), and a modulated liquid for high densities ($p \leq 1$), for which the smectic is indistinguishable from a liquid.

It is important to note the distinction between this anisotropic 2d XY melting of a LFS into a LSm and an analogous type–I melting mechanism of Ostlund and Halperin (1981) for melting of uniaxially anisotropic, but substrate-free 2d solids. In the later case, thermal fluctuations destabilize the resulting 2d smectic by further unbinding type–II dislocations, asymptotically converting it into a liquid. In contrast, because of the pinning potential, type–II dislocations remain bound by a linear potential. The resulting LSm phase is therefore distinct from the modulated liquid, in which type–II dislocations are also unbound, and separated from it by a thermodynamically sharp phase transition.

A floating solid can melt *continuously* via unbinding of the type–I dislocations. However, in contrast to the similar melting of a locked floating solid, discussed above, here the dislocation unbinding in the displacement u_y proceeds in the presence of another spectator massless phonon mode u_x, which is coupled to it. Consequently, this transition is a *nontrivial* extension of the Kosterlitz-Thouless theory and constitutes a new universality class (Frey et al. 1999; Radzihovsky et al. 2001). Once these type–I dislocations unbind the most likely resulting phase is the floating smectic.

3.3.4 Creation of substrate potentials with interfering laser beams

Substrate potentials for colloidal monolayers can be created with different techniques. Probably the most obvious method is to pattern substrates by photolithography which results in topographically patterned surfaces (see e.g. the article by van Blaaderen et al. (1997)). For systematic investigations of substrate induced phase transitions, however, it is much more convenient to create substrate potentials with optical tweezers which have been originally introduced by Ashkin (Ashkin 1970). The principle of such optical traps is in the framework of geometrical optics simply based on momentum transfer from photons – typically emitted from a laser source – which are reflected and refracted by a trapped particle to the particle itself. The net effect is that colloids with an index of refraction $n_{\rm p}$ which is larger than water ($n_{\rm w} = 1.33$) are attracted into the region of highest intensity. Optical forces acting on colloidal particles are usually divided into two categories: scattering and gradient forces. The scattering force is proportional to the light intensity and acts in the direction of the light propagation (light pressure) whereas the gradient force acts along the intensity gradient of the light pattern. Compared to topographic patterns, optical laser tweezers offer two major advantages: firstly,

the periodicity of the potential can be conveniently controlled by the geometry of the incident light pattern. This allows an *in situ* variation of the lattice constant of the substrate relative to the interparticle distance of the colloidal monolayer. Secondly, the substrate strength can be tuned with the intensity or the polarization of the incoming beams. Spatially extended light fields are conveniently created by e.g. interfering laser beams (Chowdhury et al. 1985), acousto-optic deflectors (Visscher et al. 1996) or by holographic elements (Grier 2003).

In the following, we will follow the work of Loudiyi and Ackerson (1992) who explicitly calculated the light potential V(x) resulting from the gradient forces of two laser beams with wavelength λ which interfere at an angle Θ (see Fig. 3.1). In the central region one obtains

$$V(x) \;=\; -V_0 \left[1 + \cos\left(\frac{2\,\pi\,x}{d}\right)\right] , \tag{3.53}$$

with V_0 the potential amplitude and $d = \frac{\lambda}{2}\sin\left(\frac{\Theta}{2}\right)$ the fringe spacing.

Because this expression does not take into account the finite colloidal diameter σ, integration over the potential contributions for each infinitesimal volume element of the colloidal particle is needed to obtain the effective potential acting on the whole particle. The integration is essentially a Fourier transform of a spherical volume and the resulting amplitude equals the form factor for a sphere in the Rayleigh-Gas-Debye model (Kerker 1969)

$$V_0 \;=\; 6 n_W^2 \sigma^3 \frac{P}{c r_0^2}\left[\frac{n^2-1}{n^2+2}\right]\left[\frac{j_1(\pi\sigma/d)}{2\pi\sigma/d}\right] . \tag{3.54}$$

Here, P is the laser power, c the velocity of light in vacuum, $n \;=\; n_{\mathrm{p}}/n_{\mathrm{w}}$, j_1 the first-order spherical Bessel function, and r_0 the waist radius of the Gaussian laser beam. Indeed, this is in

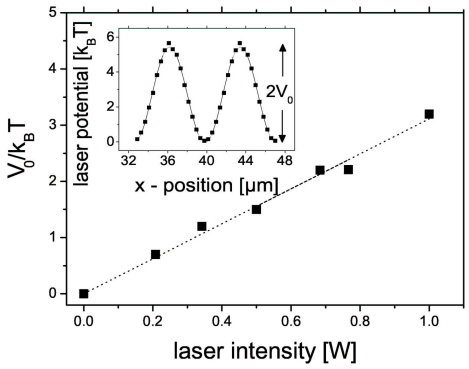

Figure 3.12: Amplitude of the light potential acting on a colloidal particle of 3μm diameter as a function of the incident laser intensity. The symbols correspond to measured data and the dashed line to a theoretical description. The inset shows the cross section of the spatially modulated laser potential experienced by the particles.

good agreement with experimental results where a highly diluted colloidal suspension (where higher order interactions can be ignored) was interacting with a 1d, periodic laser field. In

thermal equilibrium the probability distribution yields directly $V(x)$ which is shown in the inset of Fig. 3.12 and is in good agreement with Eq. 3.54. Fig. 3.12 also demonstrates the linear dependence of V_0 as a function of the incident laser intensity (Bechinger et al. 2001).

As mentioned above, due to the vertical component of the incident laser beams the colloids are also subjected to a vertical light pressure which forces the particles against the lower glass plate of the sample cell. Since both, the colloids and the glass surfaces are negatively charged when in contact with water, the light pressure is counterbalanced with the electrostatic repulsion close to the wall. From total internal reflection microscopy experiments where the particle-wall potential can be obtained, this force has been estimated to be on the order of several pico Newton (Helden et al. 2003). Accordingly, the vertical light pressure largely reduces vertical particle fluctuations and thus confines the system effectively into a 2d plane with out-of-plane fluctuations on the order of 100 nm.

The principle of interference patterns can be also extended to 2d patterns. Depending on the number and relative angles between the incoming laser beams, square, triangular, rhombic, rectangular and oblique lattices , corresponding to the full set of Bravais lattices in 2d, can be obtained (Escuti and Crawford 2004). In case of e.g. five laser beams, even quasicrystalline substrate potentials can be produced (Burns et al. 1990).

In addition to the substrate potential, the particle density is also a crucial parameter. In principle, it can be controlled by the amount of colloidal suspension in the sample cell. This, however, is often not reproducible and does not yield accurate results. A better approach is to create a well-defined boundary box around the region of interest. This is achieved by a single focused beam of an Argon-ion laser ($\lambda = 514\,\text{nm}$) which is deflected by a two-axis galvanostatic driven mirror unit (SCANgine, Germany). This allows to steer the focus around the central region of the sample with a frequency of $300\,\text{Hz}$ which results in a quasi-static optical trap which acts as a boundary box (Fig. 3.13).

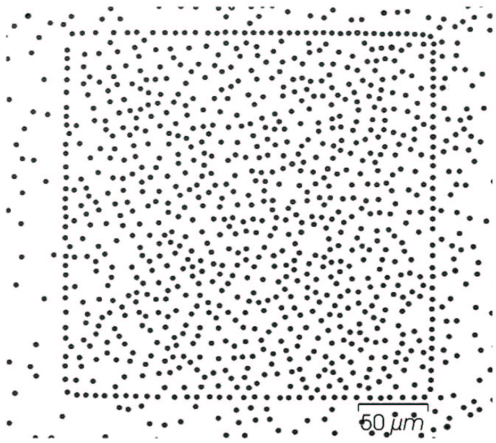

Figure 3.13: Optical image of the 2d colloidal suspension. In addition a scanned optical tweezer (not visible) creates a boundary box which allows to create a 2d colloidal system with a well-defined density. The bar corresponds to 50μm.

Depending on the size of this box, laser intensities between $100\,\text{mW}$ and $500\,\text{mW}$ were

required which result in an optical trapping potential of about $30\,k_BT$ which is needed to counterbalance the electrostatic pressure of the confined particles. This setup allowed to adjust the particle density with an accuracy of less than 1 %.

It should not go unnoticed, that this flexibility with respect to the geometry and strength of the substrate achieved in colloidal systems is hardly achieved in atomic systems, where changes in the substrate geometry are often accompanied by a change in the atomic composition. This flexibility also applies to the substrate strength which is in atomic systems dictated by the choice of substrate and adsorbate materials.

3.3.5 Density and pair correlation functions

In their pioneering work, Chowdhury et al. (1985) subjected a 2d system of charge stabilized colloidal particles to a 1d periodic laser potential created by two crossing laser beams of an Argon-ion laser. The ratio between the mean particle distance and the spacing of the laser troughs corresponded to a commensurability ratio of $p = 1$. They observed that above a critical laser intensity, periodic density modulations not directly stimulated by the periodic substrate potentials emerge which is the characteristic signature of laser-induced freezing as discussed above. Rather than discussing those experiments in detail, in the following we will describe the experiments of Wei et al. (1998), where not only crystallization but also subsequent remelting at even higher intensities was demonstrated. These experiments were also performed with an aqueous suspension of colloidal polystyrene particles with $\sigma = 1.5\,\mu$m radius. Due to surface sulfate groups, the spheres are negatively charged when in contact with water and interact via a screened Coulomb potential given by an expression derived by Derjaguin and Landau (1941) and Vervey and Overbeek (1948)

$$\Phi(r) \;=\; \frac{(Z^*\,e)^2}{4\,\pi\epsilon_{\rm P}\epsilon_0}\left(\frac{\exp(\kappa\sigma)}{1+\kappa\sigma}\right)\frac{\exp(-\kappa r)}{r}\,, \tag{3.55}$$

which is abbreviated as DLVO potential. Here Z^*e is the renormalized charge of the colloids, $\epsilon_{\rm P}$ is the dielectric constant of water and κ the inverse Debye screening length . The suspension was contained in a glass cuvette (fused silica) with $200\,\mu$m spacing. In order to control the salt concentration of the suspension, the sample cell was connected with Teflon tubings to a closed circuit consisting of a peristaltically driven pump, a vessel with ion exchange resin, and an electrical conductivity probe. With such a deionization circuit one can obtain Debye screening lengths up to about $450\,$nm. This value was determined from independent pair interaction measurements which have been carried out in the absence of periodic substrate potentials (Brunner et al. 2002). The periodic laser field was achieved by two crossing linearly polarized beams of a frequency doubled Nd:YVO_4 solid state laser with a wavelength $\lambda = 532\,$nm and an output power $P = 2\,$W. In all experiments, the particle density was below (typically $5\,$%) the critical value required for spontaneous crystallization. Accordingly, the system is in a liquid state in the absence of a light potential.

Commensurability ratio p=1

In order to quantify the order in the colloidal system two central quantities are the density $\rho(\mathbf{r})$ and the pair correlation function $g(\mathbf{r})$, theoretically defined as ensemble averages

$$\rho(\mathbf{r}) = \sum_{i=1}^{N} \langle \delta(\mathbf{r} - \mathbf{r}_i) \rangle \tag{3.56}$$

$$g(\mathbf{r}) = \frac{V}{N^2} \sum_{i,j}{}' \langle \delta(\mathbf{r} - (\mathbf{r}_i - \mathbf{r}_j)) \rangle \tag{3.57}$$

where $\mathbf{r}_i$ is the position of particle $i = 1,\ 2, \cdots, N$, and the double sum excludes the diagonal terms with $i = j$. Experimentally these quantities are obtained with video microscopy which allows to track the particle positions with a spatial resolution of about 20 nm (Baumgartl and Bechinger 2005). The experimental results for these quantities are displayed in Fig. 3.14 for a range of laser intensities. For $V_0 = 0$ the particle density $\rho(x, y)$ is rather structureless, and the pair correlation function $g(x, y)$ shows concentric rings with the typical radial profile expected for an isotropic fluid. The distance of the first ring in the pair correlation function corresponds to the mean particle distance and is in this experiment $d_{nn} = 8.6\,\mu$m. When applying a 1d, periodic laser potential in y-direction with a periodicity of $d = 7.4\,\mu$m (meeting the commensurability criterion of $a' = d$) the colloidal system undergoes a considerable structural change. Even a rather small potential amplitude of $V_0 = 0.6\,k_BT$ breaks the isotropy of the system and leads to a pronounced deviation from an isotropic liquid (Fig. 3.14 c,d). The resulting density modulation corresponds to the symmetry of the underlying substrate potential and the pair correlation function exhibits only local order while it is rather smeared out along the laser troughs as is typical for a liquid. Therefore this phase is clearly identified as the modulated liquid. Increasing the potential to $V_0 = 2.1\,k_BT$ leads to a transition to the locked floating solid which exhibits now strong modulations in ρ in both directions (Fig. 3.14 e,f). If the laser potential is further increased to $V_0 = 10\,k_BT$ the particles become even more confined to the potential minima (Fig. 3.14 g,h). This, however, does not lead to a more stable crystalline phase, as one might expect at first glance, but to a complete loss of crystalline order along the laser lines. Similar as in Fig. 3.14 a,b, the particle densities and the pair correlation functions do not show any indication of quasi-long-range order in y-direction. Obviously the system remelts to the modulated liquid state (light-induced melting, LIM).

More evidence for the assignment of the different phases is obtained when analyzing the pair correlation function parallel to the through direction, $g(y)$, as shown in Fig. 3.15. For the modulated liquid at $V_0 = 0.6\,k_BT$ the pair correlation function oscillates with an envelope that decays exponentially as expected theoretically. At intermediate potential strengths, the pair correlation function decays much slower and its envelope cannot be accurately described by an exponential but rather by an algebraic decay. We will discuss this further in the next subsection for $p = 2$. These observations for $V_0 = 2.1\,k_BT$ are consistent with 2d QLRO. At high potential strengths $g(y)$ again decays more rapidly and an exponential fit is more appropriate. This shows that the phases at $V_0 = 0.6\,k_BT$ and $V_0 = 10\,k_BT$ are thermodynamically identical.

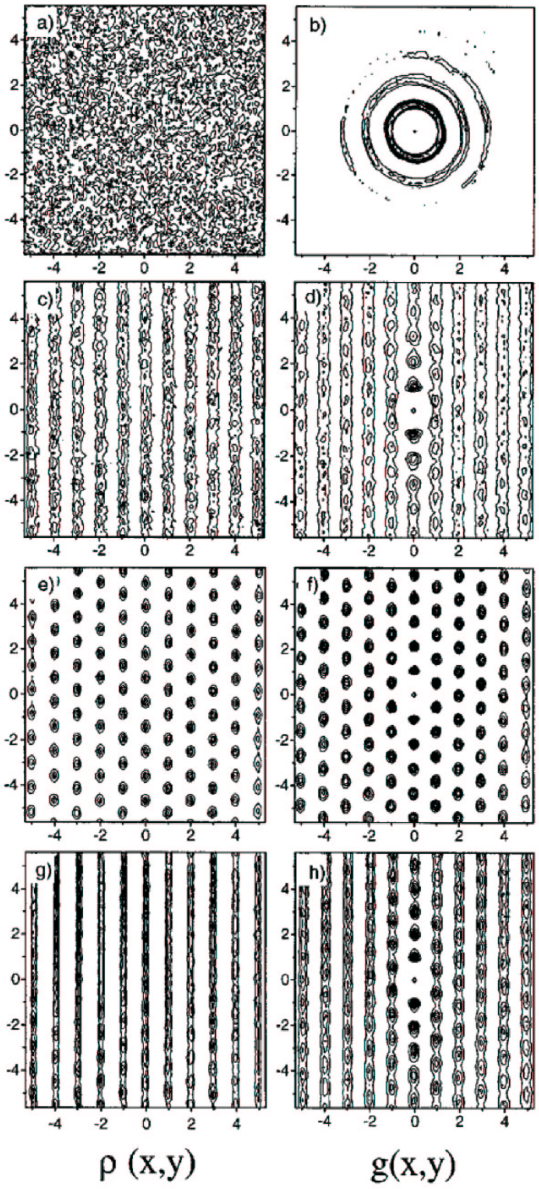

Figure 3.14: Contour plots of the averaged density distribution $\rho(x, y)$ and pair correlation function $g(x, y)$ for zero light potential [(a),(b)] and for three nonzero potential values [(c),(d)] $0.6\,k_BT$ modulated liquid, [(e),(f)] $2.1\,k_BT$ crystal, and [(g),(h)] $6.3\,k_BT$ reentrant modulated liquid. The horizontal and vertical axes are x and y, respectively. All length scales are normalized by the potential period d.

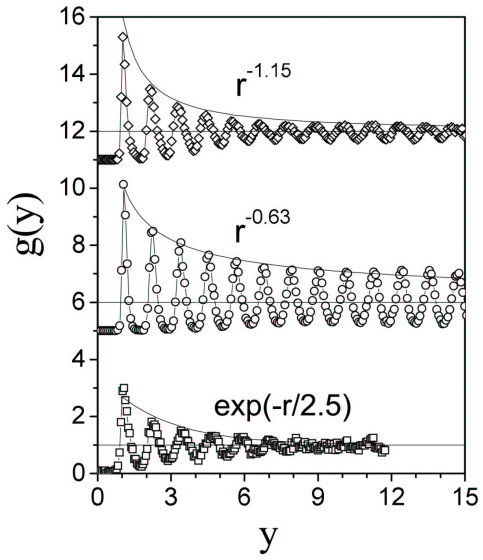

Figure 3.15: Averaged pair correlation function $g(y)$ of particles along the potential lines for $V_0 = 0.6\,k_BT$ (squares), $2.1\,k_BT$ (circles), and $6.3\,k_BT$ (diamonds), respectively. The lines are fits as explained in the text. The data are offset in the vertical direction for clarity.

Experimental results for commensurability ratio p=2

Fig. 3.16 shows the 2d density distribution $\rho(x, y)$, and the corresponding pair correlation function $g(x, y)$ for the commensurability ratio $p = 2$. In this case the particle diameter was slightly smaller ($\sigma = 2.9\,\mu$m) but all other parameters as the screening length, surface charge were rather similar than above. With increasing substrate strength V_0 the particles become more and more localized along the interference fringes due to light forces. Because of the repulsive particle interaction, the system responds at sufficiently high V_0 by forming a crystalline (LFS) phase. Fig. 3.16 a shows the LFS which was obtained for $V_0 = 4.2k_BT$. This situation is very similar to the corresponding phase at $p = 1$ where due to the interplay of inter-particle and particle-substrate forces a light-induced crystalline state was observed (Chowdhury et al. 1985; Wei et al. 1998). In contrast to $p = 1$, however, here on average only every second row is occupied with particles. The corresponding $g(x, y)$ in Fig. 3.16 b supports the characteristic QLRO of the LFS along the potential troughs which is responsible for the non-zero shear elasticity. Upon increasing the laser potential to $V_0 = 7.9k_BT$ the particle density shows a different structure; see Figs. 3.16 c,d. In contrast to the LFS, now only short-range correlations along the troughs are observed but the density modulation as observed for the LFS perpendicular to the troughs is still preserved. It is important to realize that even at $V_0 = 7.9k_BT$ the potential barriers between the troughs are sufficiently small to be overcome by the particles (as is observed in the experiment). Therefore, the structure presented in Figs. 3.16 c,d is an equilibrated state being identified as the LSm phase. Both, the existence of the LSm and in

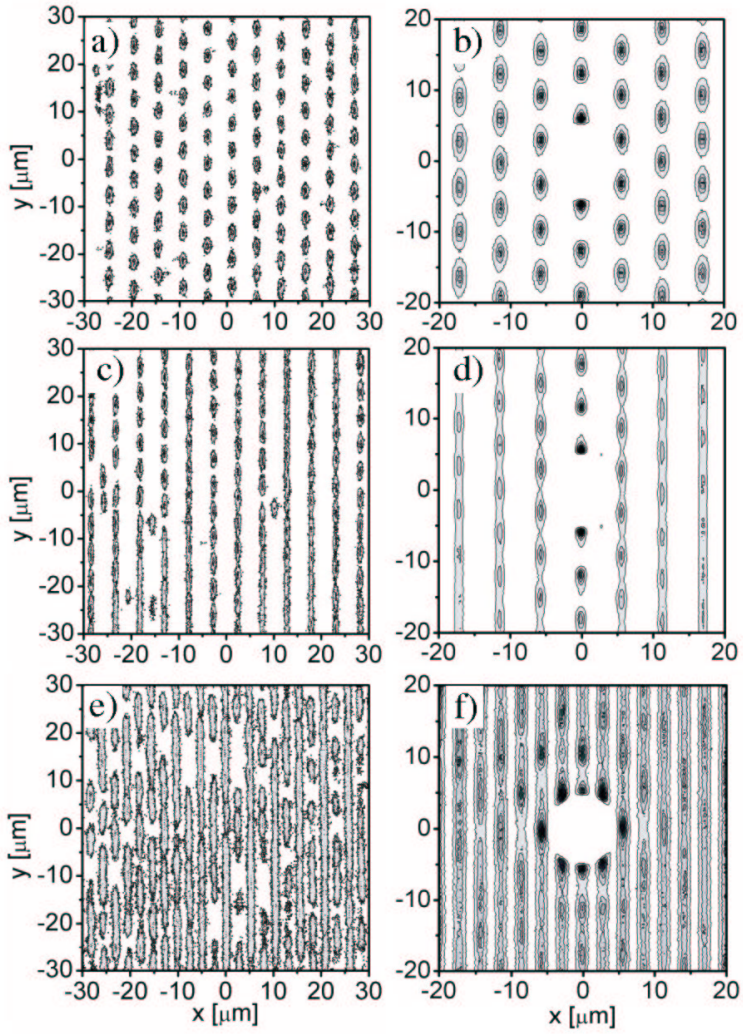

Figure 3.16: Contour plots of the averaged particle density $\rho(x, y)$ and pair correlation function $g(x, y)$ for (a, b) LFS, (c, d) LSm and (e, f) ML phase.

particular the transition from the LFS to the LSm upon increasing V_0 is in agreement with theoretical predictions (Frey et al. 1999; Radzihovsky et al. 2001). Theory also suggests that further increase of the laser potential leads to a transition from the LSm to a modulated liquid. This is caused by a reduction of the particle fluctuations perpendicular to the laser troughs, thus decreasing the effective interaction among particles in neighboring troughs. Accordingly, for short-range pair potentials (as discussed here) the interaction energies of the LSm and the ML

in the limit of large V_0 are approximately the same. However, due to entropic contributions the free energy of the ML (where the particles are randomly distributed across *all* potential troughs) becomes smaller and a transition from the LSm to the ML should occur (Frey et al. 1999; Radzihovsky et al. 2001). Due to kinetic reasons, such a transition is not observed in experiments because the LSm to ML transition requires the thermally activated surmounting of particles across the laser troughs. The high V_0 values required for this transition strongly suppress such barrier crossings and therefore, a light-induced LSm-ML transition is not expected to occur on experimental time scales with the above system parameters. According to the theoretical considerations discussed above the transition from the LSm to the ML should also be observed when reducing the pair-interaction energy (Frey et al. 1999). This was experimentally achieved by increasing the salt concentration in the suspension, i.e. decreasing the Debye screening length . Fig. 3.16 e,f shows the data obtained at a lower screening length (about $\kappa^{-1} \approx 450\,\mathrm{nm}$) and a substrate strength of $V_0 = 6.7 k_B T$. As can be seen, now all potential troughs are occupied with particles which is a clear signature of the ML. Similar to the case $p = 1$ (Wei et al. 1998) local hexagonal order is observed while correlations along the y-direction rapidly decay (Fig. 3.16 f).

Similar as above, a more quantitative description of the phases is obtained from the pair correlation function along the laser lines $g(y)$. Fig. 3.17 shows the corresponding curves for the LFS phase (squares) which exhibits quasi long-range order along the troughs. Theoretically, one expects that both leading and subleading contributions have to be taken into account for the analysis of the pair correlation function (Frey et al. 1999; Radzihovsky et al. 2001)

$$g(y) - 1 \;=\; const. + g_A \cos(G_y^0 y) y^{-\eta_{G_{A,y}}} + g_B \cos(2G_y^0 y) y^{-\eta_{G_{B,y}}}\,, \tag{3.58}$$

where $G_y^0 = 2\pi/a$, $g_{A,B}$ are amplitudes depending on the strength of the laser potential, and the exponents are given by $\eta_{G_{A,y}} = \frac{1}{4}$ and $\eta_{G_{B,y}} = 1$ at the transition temperature. The constant term reflects the effect of the laser potential to induce a periodic modulation of the colloidal particle density with a higher density in the minima of the troughs. Note that this trivially implies that the pair correlation function does *not* approach unity as $x \to \infty$ if $g(y)$ is normalized with respect to the mean density. Due to the superposition of the two harmonics with different power-law amplitudes the minima are much broader than the maxima of the structure factor; see Fig. 3.18. Indeed, Eq. 3.58 which is plotted as the solid line describes the experimental data of Fig. 3.17 very well, in particular the flattened minima are reproduced; we did not try to fit the first peak because it critically depends on the pair potential between the particles which is not taken into account by Eq. 3.58. A least mean square fit to the data yields $\eta_{G_{A,y}} = 0.27$ and $\eta_{G_{B,y}} = 1.19$ which suggests that the observed LFS is close to the melting point (Frey et al. 1999; Radzihovsky et al. 2001). For comparison, the peaks in $g(y)$ are also fitted with a single algebraic fit (solid line in Fig. 3.17). Although it describes the data very well and indeed also supports a solid phase, the resulting exponent has to be taken with care (Frey et al. 1999; Radzihovsky et al. 2001). The pair correlation functions of the LSm (triangles) and the ML phase (circles) decay much faster and the envelope at larger distances is best described by a single exponential as seen by the solid line in Fig. 3.17 (an algebraic fit according to Eq. 3.58 yields $\eta_{G_{A,y}} \geq 1$ which is beyond the limiting value indicating QLRO). This clearly demonstrates the short-ranged nature of correlations along the potential troughs in this phase. In the ML phase the correlation function decays even faster and becomes rather

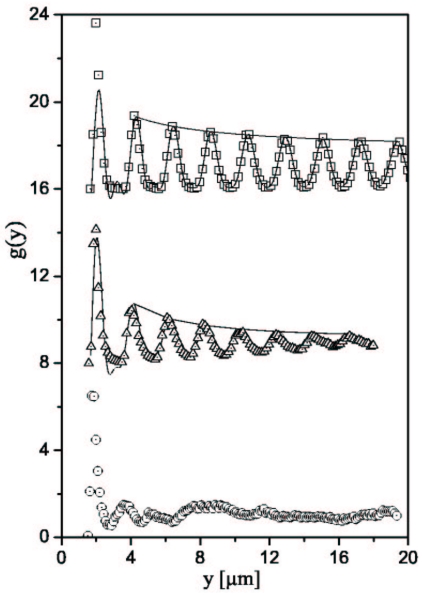

Figure 3.17: Pair correlation functions $g(y)$ along the potential troughs for LFS (squares), LSm (triangles), and the ML phase (circles), respectively. The data are displaced in vertical direction for clarity. The solid lines are fitting functions as explained in the text.

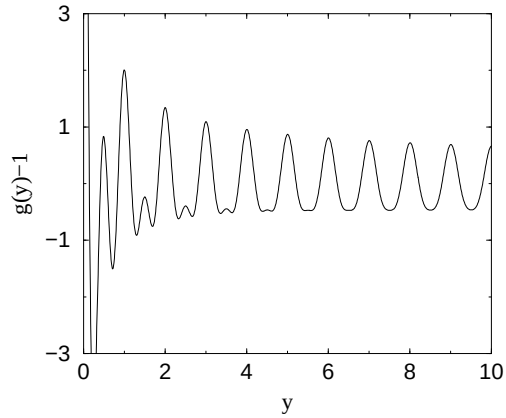

Figure 3.18: Algebraic part of the pair correlation function along the laser troughs. There are two oscillating contributions, both of them decay algebraically to zero.

noisy beyond distances of $6\,\mu$m. This very fast decay is essentially caused by the largely

reduced coupling of particles in adjacent lines.

3.3.6 Reentrance melting

One of the most interesting observations in the colloidal experiments described above is the phenomenon of light-induced *reentrant* melting . This phenomenon is a *generic* consequence of short-ranged screened colloidal interactions and thermal fluctuations, and hence should be prevalent in such 2d systems (Frey et al. 1999). Since the LFS-ML, LFS-LSm and FS-FSm transitions are all driven by the unbinding of type–I dislocations, the following arguments apply equally well to all of them. Let $T_{\rm m}(V_0)$ denote the melting temperature as a function of the potential strength. Then these melting boundaries $T_{\rm m}(V_0)$ are constrained by their limiting values

$$T_{\rm m}(0) = \frac{b_{\vec{n}}^2}{4\pi}\frac{\mu(\mu+\lambda)}{2\mu+\lambda} , \tag{3.59}$$

$$T_{\rm m}(\infty) = \frac{b_{\vec{n}}^2}{8\pi}\sqrt{\mu(2\mu+\lambda)} , \tag{3.60}$$

where $T_{\rm m}(0)$ is the well-known result in the absence of an external potential (Kosterlitz and Thouless 1973; Nelson and Halperin 1979; Young 1979). In the opposite limit of *infinite* potential strength, $T_{\rm m}(\infty)$ is given by Eq. 3.52, with $B_{yy}(V_0 \to \infty) \approx 2\mu+\lambda$ and $B_{xy}(V_0 \to \infty) \approx \mu$. Although, in general, there is no universal relation between $T_{\rm m}(0)$ and $T_{\rm m}(\infty)$, in the dilute colloidal limit, relevant to the experiments of Wei *et al.* (Wei et al. 1998), the two Lamé coefficients are expected to be roughly equal, $\mu \approx \lambda$, and Eqs.3.60 reduce to

$$T_{\rm m}^{\rm dil}(0) = \frac{b_{\vec{n}}^2}{6\pi}\,\mu , \tag{3.61}$$

$$T_{\rm m}^{\rm dil}(\infty) = \frac{b_{\vec{n}}^2}{8\pi}\,\sqrt{3}\mu \approx 1.3\,T_{\rm m}^{\rm dil}(0) . \tag{3.62}$$

A first guess would be that the melting temperature simply increases monotonically with V_0 from $T_{\rm m}(0)$ to $T_{\rm m}(\infty)$. However, as explained below, the thermal fluctuations perpendicular to the trough direction, enhanced as the periodic potential is *lowered* from infinity, generically *increase* the melting temperature for $\kappa a \gg 1$. Consequently, the melting curve, $T_{\rm m}(V_0)$, must have a maximum in this limit, implying reentrant melting for a band of temperatures as a function of the potential amplitude.

The origin of the reentrance effect can be understood on a heuristic level as follows. Clearly, at *small* V_0, one expects that the increase in the strength of the periodic potential suppresses thermal fluctuations in u_x, thereby lowering the entropy of the liquid (or the smectic) state, and therefore making freezing into a lattice free-energetically less costly. This naturally leads to an *increase* of $T_{\rm m}(V_0)$ with V_0 at low laser intensities. However, for potential strengths $V_0 \gg k_B T$, this entropic contribution to the free energy becomes unimportant. In this large V_0 limit, the behavior of $T_{\rm m}(V_0)$ is dominated by a different mechanism having to do with the reduction of the elastic constants with increasing V_0 and decreasing temperature. To see this, note that the effective shear modulus $B_{xy}(V_0)$ which enters $T_{\rm m}(V_0)$ is determined by the screened Coulomb interaction between colloidal particles in neighboring troughs. In order to find an effective shear modulus for the modes parallel to the laser troughs, one needs to

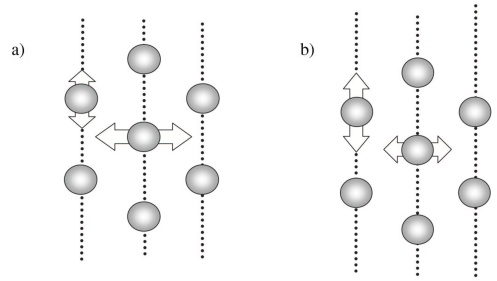

Figure 3.19: Schematic illustration of how fluctuations affect the particle interaction in neighboring minima of the laser potential (dashed lines). The vertical and horizontal arrows denote the strength of the particle interactions perpendicular and along the laser potential. (a) In the solid phase particle fluctuations perpendicular to the interference pattern contribute to the registration of adjacent lines. (b) At higher light intensities those particle fluctuations are reduced by the laser field and thus lead to a reduced coupling of adjacent lines which then leads to the reentrant modulated liquid phase.

integrate out the massive modes corresponding to displacements perpendicular to the troughs of the laser potential. Heuristically, one should get roughly the same result by assuming that the dominant effect comes from the shear modulus B_{xy} and simply averaging the potential over the massive u_x degrees of freedom, which yields

$$B_{xy}(V_0) \sim \langle e^{-\kappa|\mathbf{r}_{n+1}-\mathbf{r}_n|}\rangle_{u_y} \ . \tag{3.63}$$

Here $\mathbf{r}_n$ and $\mathbf{r}_{n+1}$ are positions of nearest neighbor colloidal particles belonging to the n-th and $n+1$-st Bragg planes, running parallel to the laser potential troughs. This gives to lowest harmonic order in the fluctuations u_x,

$$B_{xy}(V_0) \sim \langle e^{-\kappa a-\kappa[u_y(n+1)-u_y(n)]}\rangle \sim e^{-\kappa a}e^{\kappa^2\langle u_y^2\rangle} \approx B_{xy}(\infty)e^{ck_BT/V_0} \ . \tag{3.64}$$

with c a dimensionless number of order 1. This thermal *enhancement* of the effective shear modulus $B_{xy}(V_0)$, which decreases as thermal fluctuations in u_x are suppressed by increasing V_0, is illustrated in Fig. 3.19. Its physical origin is easy to understand: Even though, in the presence of u_x fluctuations colloidal particles in neighboring troughs spend as much time closer together as further apart, because of the concave form of the interaction potential the enhancement of the effective shear modulus is larger from particles being closer together than the corresponding suppression when they are further apart. These simple physical arguments for reentrance are supported by detailed microscopic lattice calculations (Frey et al. 1999; Radzihovsky et al. 2001). Explicitly one finds

$$T_{\rm m}(V_0) = T_{\rm m}^{\infty}\left\{1+\frac{5[(\kappa a)^2-31]}{64\pi^2}\left(1+\frac{13}{3\kappa a}\right)\frac{k_BT_{\rm m}^{\infty}}{p^2V_0}\right\} \ . \tag{3.65}$$

Among others this implies that $T_{\rm m}$ increases with decreasing V_0 for $\kappa a \gtrsim 5.6$. Note that this value is only a rough estimate which does not account for renormalizations by dislocation dipoles and nonlinear elastic effects. The important theoretical conclusion here is the existence of a lower bound.

Recent experimental investigations (Bechinger et al. 2001) and Monte Carlo simulations (Strepp et al. 2001b) have mapped out a detailed phase diagram in the parameter space of

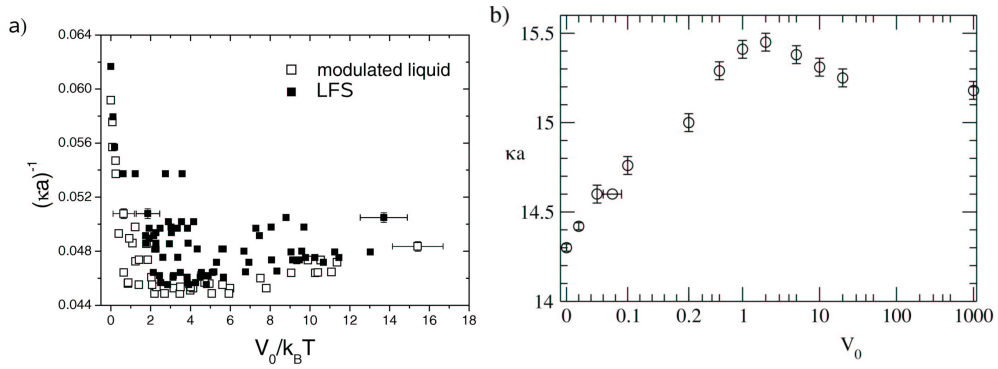

Figure 3.20: a) Experimentally determined phase diagram as a function of $(\kappa a)^{-1}$ versus V_0/k_BT. The open symbols denote the modulated liquid and the closed symbols denoted the locked floating solid phase, respectively. For clarity, error bars are plotted only for a few data points. Adapted from the article by Bechinger et al. (2001) b) Phase boundary as determined by Monte Carlo simulations of colloidal particles interacting by a DLVO potential. Adapted from the article by Strepp et al. (2001b).

V_0/k_BT and κa with temperature fixed and commensurability ratio $p = 1$. The results are illustrated in Fig. 3.20 a and b, respectively. The experimental parameters were as follows (Bechinger et al. 2001): colloidal particles of diameter $2\sigma = 3\,\mu$m, effective charge $Z^* = 20000$, and Debye screening length $\kappa^{-1} \approx 400\,$nm. As can be seen from Fig. 3.20 a, the value of $(\kappa a)^{-1}$ where the transition towards the LFS occurs decreases at small laser intensities as a function of V_0. This is the characteristic of light induced freezing. For larger values of V_0, however, the separation line between the solid and the modulated liquid is shifted back to higher $(\kappa a)^{-1}$ values and starts to saturate at the highest value which was obtained within the experimental setup (Bechinger et al. 2001). It is this up bending which gives rise to the light induced melting phenomenon. If $(\kappa a)^{-1}$ is in a range between 0.045 and 0.048, with increasing V_0 one observes a reentrant melting phenomenon. The Monte Carlo data presented in Fig. 3.20 b were obtained for the following parameters (Strepp et al. 2001b): system size $N = 1024$, colloidal particles of diameter $2\sigma = 1.07\,\mu$m, effective charge $Z^* = 7800$, lattice constant $a \approx 2.5\,\mu$m, and $\epsilon_{\rm P} = 78$. As reported by Strepp et al. (2001b) the results did not change significantly upon using parameters which are closer to the experimental values quoted above. The experimental and numerical phase diagrams have the same shape, but the experimental phase diagram shows larger freezing and reentrance regions and is shifted to higher values of κa at about a magnitude of 4.5 on average. The reason for this difference may be due to the particle interaction. Whereas the simulations use a strict DLVO pair potential, there is evidence for three-body interactions in collodial systems (Brunner and Bechinger 2002).

In agreement with experimental data (Wei et al. 1998; Bechinger et al. 2001) and theory (Frey et al. 1999; Radzihovsky et al. 2001) the detailed analysis of the Monte Carlo simulations (Strepp et al. 2001b) shows several features consistent with a dislocation mediated melting mechanism. This seems to settle a debate with earlier simulations, which were controversial and remained inconclusive. While the first simulations (Chakrabarti et al. 1995) found evidence for a change from a first-order to a continuous transition at some intermediate

laser intensities, later studies refuted these results (Das et al. 1998; Das et al. 1999; Das et al. 2001). Actually, a tricritical point was originally also predicted within Landau theory (Chowdhury et al. 1985) and density functional theory (Chakrabarti et al. 1994). Though these early theoretical results have played an important role in motivating experimental and numerical research, there is now – as discussed above – a large body of evidence in favor of a dislocated mediated mechanism, whose predictions will be summarized next.

Since the melting temperature is proportional to the elastic moduli, which in turn are proportional to the potential strength, for $\kappa a \gg 1$ one expects T_m to display the following dependence on the screening length $T_\mathrm{m} \propto (\kappa a)^2 e^{-\kappa a}$. As an immediate consequence one gets (in the dilute limit) the following implicit equation (Radzihovsky et al. 2001)

$$(\kappa_\mathrm{m}^\infty - \kappa_\mathrm{m}^0)a \approx 2\ln\left(1.3\frac{\kappa_\mathrm{m}^\infty}{\kappa_\mathrm{m}^0}\right) > 0\ . \tag{3.66}$$

In particular this implies that the difference in the critical values of the inverse screening length at infinite and zero potential strength, κ_m^∞ and κ_m^0, is positive. In the limit $\kappa_\mathrm{m}^0 a \gg 1$, Eq. 3.66 reduces to $(\kappa_\mathrm{m}^\infty - \kappa_\mathrm{m}^0)a \approx 2\ln 1.3 \approx 0.52$. This estimate is consistent with both experiments (Bechinger et al. 2001) and recent Monte Carlo simulations (Strepp et al. 2001b). The results of the early Monte Carlo simulations, however, appeared to disagree with these predictions from the dislocation-mediated melting theory when compared for large values of the potential strength. Whereas theory predicts $\kappa_\mathrm{m}^\infty > \kappa_\mathrm{m}^0$, the simulations reported by Chakrabarti et al. (1995) show quite the opposite. More recent simulations (Das et al. 1999) refute these earlier results and find in agreement with theory $\kappa_\mathrm{m}^\infty - \kappa_\mathrm{m}^0 > 0$. Their numerical value for $(\kappa_\mathrm{m}^\infty - \kappa_\mathrm{m}^0)a \approx 1.32$ is slightly larger than the later numerical result (Strepp et al. 2001b) and roughly two times larger than the theoretical estimate of 0.52. These differences are not significant for several reasons. First, since Eq. 3.66 neglects finite renormalization of elastic constants by dislocation dipoles and nonlinear elastic effects, the theoretical prediction is an estimate, only accurate up to unknown factors of order 1. Second, a common problem with all simulation studies might be equilibration with respect to dislocation climb or glide.

Next we discuss reentrance in the V_0/k_BT-$\kappa_\mathrm{m}a$ phase diagram. Upon rewriting Eq. 3.65 one finds

$$\frac{V_0}{k_BT} = \frac{\alpha(\kappa_\mathrm{m}a)}{T/T_\mathrm{m}^\infty(\kappa_\mathrm{m}a) - 1} \tag{3.67}$$

with

$$\alpha(\kappa_\mathrm{m}a) = \frac{5\big((\kappa_\mathrm{m}a)^2 - 31\big)}{64\pi^2}\left(1 + \frac{13}{3\kappa_\mathrm{m}a}\right)\ . \tag{3.68}$$

Hence, if $\kappa_\mathrm{m}^0 a$ and $\kappa_\mathrm{m}^\infty a$ are both smaller than the critical value 5.6 for the existence of reentrance, one expects $(\kappa_\mathrm{m}a)^{-1}$ to be a monotonically decreasing function of the potential strength, as shown by the dashed line in Fig. 3.21. If $\kappa_\mathrm{m}^0 a$ and $\kappa_\mathrm{m}^\infty a$ are both larger than the critical value 5.6, we expect reentrant behavior such that with increasing potential strength $(\kappa_\mathrm{m}a)^{-1}$ first decreases and reaches a minimum $(\kappa_\mathrm{m}^\mathrm{min}a)^{-1} < (\kappa_\mathrm{m}^\infty a)^{-1}$ before it approaches $(\kappa_\mathrm{m}^\infty a)^{-1}$ as an inverse power of V_0 according to Eq. 3.67 (see Fig. 3.21). This reentrant behavior is consistent with the experimental results (Bechinger et al. 2001) and Monte Carlo simulations (Strepp et al. 2001b) shown in Fig. 3.20.

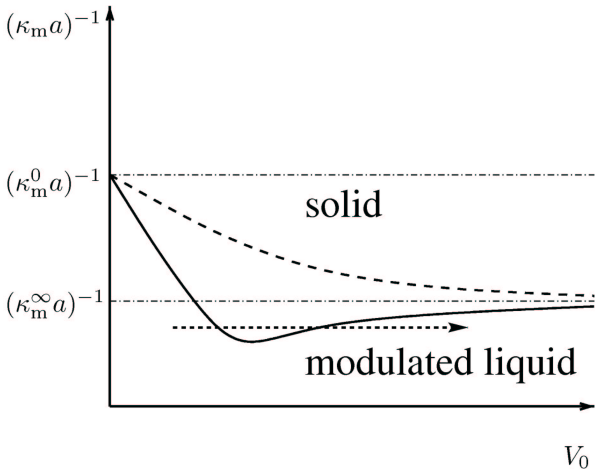

Figure 3.21: Schematic $p = 1$ phase diagram as a function of potential strength V_0 and inverse Debye screening length κ. Solid and dashed curves represent the melting curves for values of κ being larger or smaller respectively than the critical value of $\kappa_{\rm crit}a \approx 5.6$.

In summary, this shows that a defect-mediated mechanism for the reentrant melting phenomenon observed in experiment and simulations provides a consistent theoretical framework. We close this section with reviewing recent developments that make it possible to test some of the non-universal predictions of defect-mediated theories even quantitatively. The key idea is to use restricted Monte Carlo simulations not allowing for defects to calculate the values of the bare elastic constants, which then serve as input parameters for the flow equations obtained from a renormalization group analysis (Morf 1979; Fisher et al. 1979). Of course, an obvious shortcoming of this method is that the flow equations are not known exactly but only approximately. Over the years this idea has been applied to analyze defect-mediated transitions in the planar rotor model (Sengupta et al. 2000a) and 2d melting of hard disks (Sengupta et al. 2000b). More recently, it has also been used to study 2d melting in a 1d periodic potential (Chaudhuri and Sengupta 2004a; Chaudhuri and Sengupta 2004b; Chaudhuri and Sengupta 2006). In these studies it turned out to be essential to keep next to leading order corrections in the renormalization group flow equations to obtain the reentrant phase diagram. Then, for hard disks (Chaudhuri and Sengupta 2006) the phase diagram comes out to be exactly the same as found from earlier direct simulations (Strepp et al. 2001a). This provides a nice validation of the defect-mediated reentrant melting scenario (Frey et al. 1999; Radzihovsky et al. 2001). For particles interacting with a DLVO pair potential there are quantitative differences, while the qualitative form of the phase diagram is reproduced (Chaudhuri and Sengupta 2006).

3.4 Colloidal molecular crystals

Colloidal particles subject to potential patterns of 2d periodicity, generated by interfering laser beams (Burns et al. 1990) and holographic optical tweezer techniques (Grier 2003), have given us a fresh look at the phase behavior of two-dimensional systems. For example, these soft matter systems mimic (Reichhardt et al. 2001; Laguna et al. 2001; Mangold et al. 2003) the behavior of a vortex lattice interacting with a periodic pinning array (Baert et al. 1995; Matsuda et al. 1996; Martín et al. 1997); see also section 3.5.2. Perhaphs even more interestingly, they also make it possible to realize novel colloidal crystalline states. In particular, when there are more colloidal particles than potential minima, composite colloidal aggregates with internal degrees of freedom and a non-spherical overall shape may form in each of the potential minima. Fig. 3.22 shows the experimental realization of a triangular optical interference pattern and a colloidal system with a filling factor of $m = 3$, where the intensity of the laser field is taken sufficiently high such the three colloids are localized on each of the laser lattice sites. If the localization of these groups of m particles at their particular lattice site is strong enough,they may be regarded as m-mers or colloidal molecules. Then, the important low energy excitations are the orientation of the trimers, regarded as rigid composite objects, with respect to the lattice direction.

Depending on the symmetry of the potential patterns, the filling factor m and the potential strength a myriad of phases is possible. Fig. 3.23 shows crystalline ground states for square and triangular lattices of colloidal particles interacting with a screened Coulomb potential for filling factors ranging from $m = 1$ to $m = 4$. Due to their similarity to molecular crystals these states have been termed *colloidal molecular crystals* (Reichhardt and Olson 2002). In addition to a phase transition from a modulated liquid state to a crystalline state with a m-mer ("molecule") localized at each potential minimum these systems now also can exhibit transitions where the m-mers become orientationally ordered. This results in a much richer phase behavior than the well studied case of order-disorder transitions in lattice gases with filling factors $m < 1$ (Schick 1981).

In this section we will review recent theoretical and experimental progress in understand-

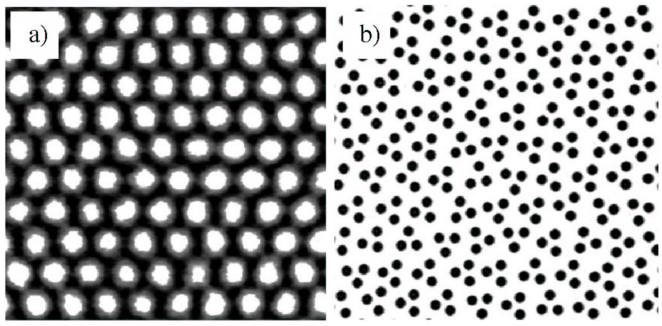

Figure 3.22: Optical images of (a) the triangular optical interference pattern which serves as the substrate potential and (b) colloidal particles which form trimers at sufficiently high substrate strengths. The region corresponds to about $100 \times 100\,\mathrm{mm}^2$.

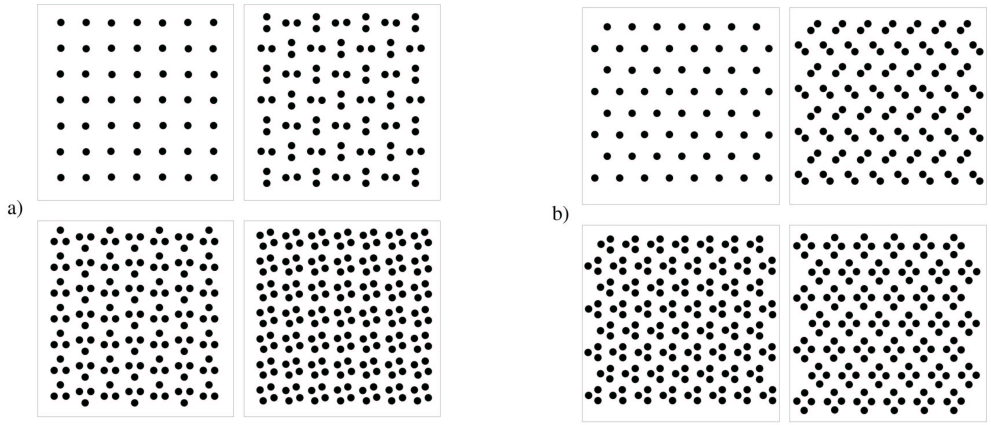

Figure 3.23: Possible ground states of colloidal particles subject to square (a) and triangular (b) 2d periodic substrate potentials; adapted from the article of Reichhardt and Olson (2002).

ing the type of ordering and transitions emerging in these colloidal molecular crystals. We will mainly focus on those systems where experimental data are available, namely dimers and trimers in triangular lattices (Brunner and Bechinger 2002). Theoretical progress in this field has been mainly along two lines. Extensive Langevin simulations have been performed to identify possible ground states and transitions between ordered states (Reichhardt and Olson 2002). The transitions between orientationally ordered and disordered states have been characterized using Monte Carlo simulations and a variety of analytical approaches (Šarlah et al. 2005; Šarlah et al. 2006). The latter progress has been facilitated by the experimental observation that the groups of colloids in each potential minimum are to be considered as rather rigid entities as soon as the laser potential exceeds several tens of $k_B T$. The key idea then is to keep only discrete orientational states of the colloidal "molecule" as fluctuating variables, i.e., the essential low-energy degrees of freedom relevant for a statistical mechanics description. Since the condensation or binding energy to build such molecules is much larger than the thermal scale, one is lead to ignore processes connected with the breaking apart of the "molecular" structure. The price to be paid for using this concept is that the theoretical description remains semi-phenomenological, i.e., it does not explain the formation of molecules. In particular, the regime of low laser intensities where the molecular crystal exhibits a significant fraction of defects is not within the scope of such an approach and has to be studied by other theoretical methods, for example upon using Langevin simulations (Reichhardt and Olson 2002). The benefit of focusing on effective low-energy excitations is that one can derive simple models that are amenable to powerful methods of the statistical mechanics toolbox. In particular, it allows to identify the appropriate broken symmetry phases and to map the problem to related magnetic transitions for which a great wealth of knowledge has been developed.

3.4.1 Colloidal trimers on triangular lattices

In the experimental investigations on colloidal systems with filling factor $m = 3$ (Brunner and Bechinger 2002) the density of colloids has been selected in a regime below the spontaneous freezing temperature on a flat substrate. Accordingly, the system is in a liquid state when no 2d light lattice is applied. Then, in order to investigate the effect of the substrate potential depth onto the structure of the colloidal system, the laser intensity was increased and the spatially resolved average particle density $\rho(x, y)$ in a central region of the interference pattern was observed. In addition, also the averaged local particle density $\rho_{\text{loc}}(x, y)$ in a substrate potential well was calculated. Both quantities are plotted as the left and right column of Fig. 3.24 respectively.

At low intensities of the lasers, corresponding to a potential depth of $V_0 = 40 k_B T$, the colloids exhibit the typical response of a fluid to an external modulation, i.e., a small periodic component is superimposed to the homogeneous background density. At these moderate substrate strengths most of the particles are still able to surmount the barriers between the substrate potential wells. Accordingly, the corresponding plot of ρ_{loc} shows a relatively even particle distribution. These are the characteristics of a *modulated liquid* phase. Enhancing the strength of the laser potential to $V_0 = 60\, k_B T$ particles become localized and essentially all of the potential wells are occupied with trimers (see Fig. 3.24). As is seen in Fig. 3.24 f, these trimers also posses a very high degree of orientational order. In addition to the three most pronounced spots which indicate the main orientation of the trimers, Fig. 3.24 f shows another three weak spots which correspond to defects where the orientation of trimers is rotated by 60 degrees. These two orientations correspond to the twofold degenerate ground state of the system, which is already pointing towards an Lenz-Ising symmetry of this *orientationally ordered* state. When the substrate strength is further increased to $110\, k_B T$, the centers of the trimers become more localized at the lattice sites of the interference pattern. In contrast to the enhanced positional order, however, the orientational order of the trimers becomes much weaker as is seen from the ring-shaped density distribution in Fig. 3.24 g. This is supported by Fig. 3.24 h which shows that the orientation of the trimers is more diffuse in angular direction. These results clearly demonstrate that increasing the depth of the potential wells leads to a loss of orientational order between the trimers.

This interesting set of experimental findings can be explained quantitatively in the limit of strong laser potentials. Then the low-energy effective degrees of freedom are given by the discrete orientational states of the composite object, here trimers. Due to the symmetry of the optical lattice the trimers constitute equilateral triangles which are aligned with the triangular pattern. From Fig. 3.25 one infers two energetically equivalent orientational states of the trimer corresponding to the optimal balance between the compression of the constituent colloids due to the laser potential and their mutual screened Coulomb repulsion. Each of these states, $S = \pm 1$, consist of three equivalent orientations obtained by 120° rotations. The residual interaction between trimers depends on their relative orientation as well as on their relative lattice position. Since the residual interaction is solely due to a screened Coulomb interaction the magnitude of this energy decreases rapidly with increasing distance. For typical experimental setups the screening length is an order of magnitude smaller than the lattice constant, which allows to restrict the residual interaction to nearest neighbors. For each neighboring pair of trimers there are then four possible geometrical configurations, two of which are mir-

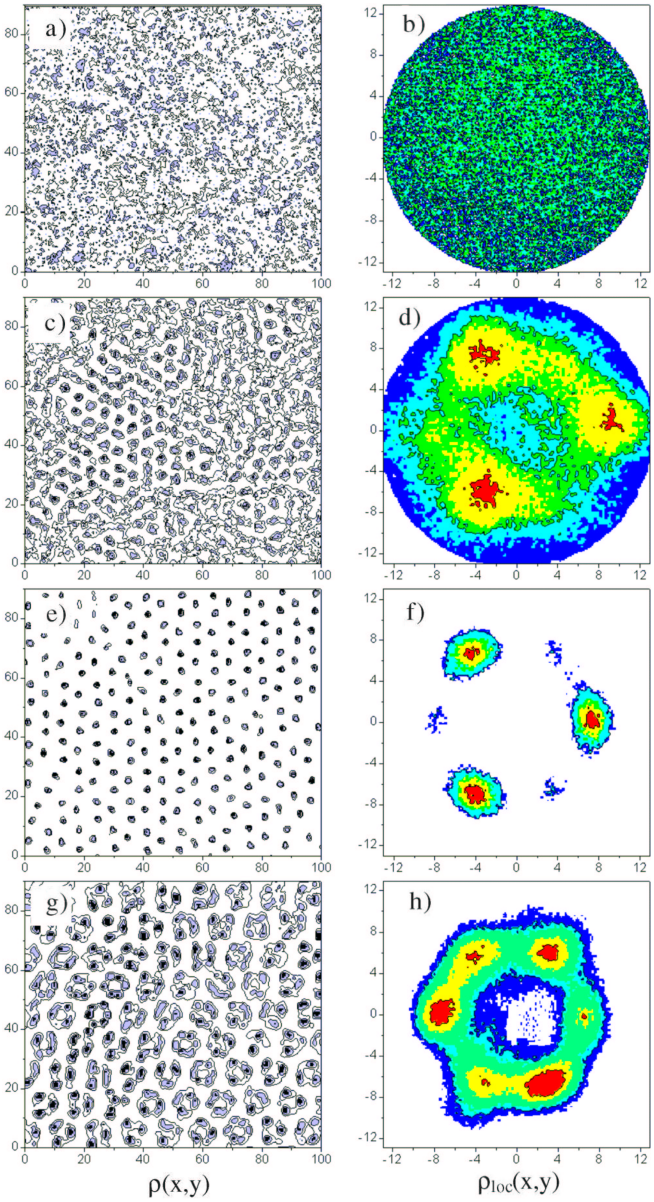

Figure 3.24: Contour plots of the lateral density distribution ρ and the averaged local particle density ρ_{loc} for different light potentials V_0: (a),(b) $0\,k_BT$, (c),(d) $40\,k_BT$, (e),(f) $60\,k_BT$, and (g),(h) $110\,k_BT$. The horizontal and vertical axes are x and y, respectively. All units are in mm.

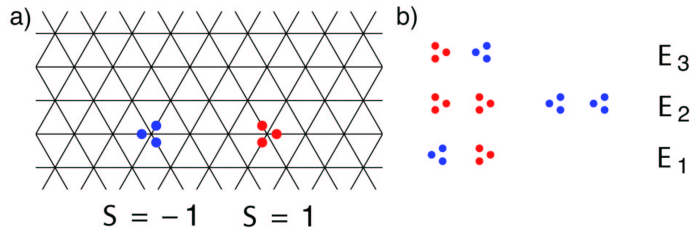

Figure 3.25: Lattice gas model (a) The triangular lattice of the external field and the two discrete orientational states of the trimers. (b) Three interaction energies for the orientational configurations of neighboring trimers.

ror images of each other, see Fig. 3.25 b. These configurations introduce three energy scales, with generic ordering $E_1 < E_2 < E_3$. Since a global shift of the energy scale does not affect the phase diagram, this leaves two independent energy differences. These scales are functions of the screening length, the strength of the laser potential, as well as the effective charges of the constituent colloids; for a detailled discussion see Šarlah et al. (2006).

Introducing the thermal scale k_BT allows to construct two dimensionless parameters out of the two energy differences, and naively one would expect a two-dimensional phase diagram. However, it can be shown that due to geometrical constraints a local spin flip generates an energetic excitation that can be expressed in terms of a single energy scale for all possible configurations of the neighboring trimers (Šarlah et al. 2006). This may be seen as follows. Consider three colinear trimers, i.e., the smallest neighborhood of trimers with representatives of both inequivalent bond orientations. Upon fixing the central trimer there are 2^2 possible configurations of the two neighbors, all of them are depicted in Fig. 3.26 (a). Then, flipping the central trimer yields the energy changes $\pm\Delta E$, 0 where we have defined $\Delta E \equiv E_1 + E_3 - 2E_2$. Although unexpected due to the bond-oriented local interaction energies, the trimer system reduces to an Lenz-Ising model, i.e., with spins allowing for two distinct orientations

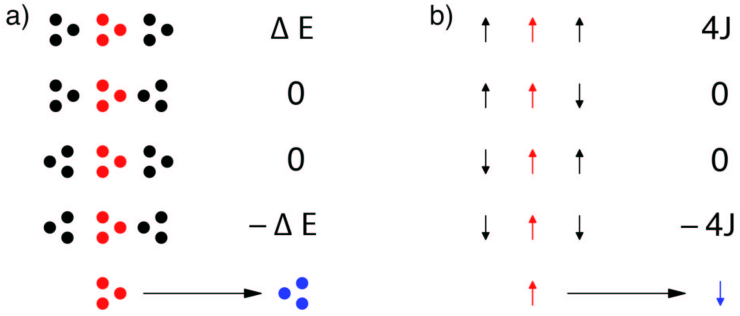

Figure 3.26: (a) Schematic representation of all possible situations for a trimer flip with the corresponding energy changes; $\Delta E = E_1 + E_3 - 2E_2$. (b) The same as in (a) but for spins of the spin-$1/2$ Lenz-Ising Hamiltonian $\mathcal{H}_{LI} = -J\sum_{\langle ij\rangle} S_iS_j$.

and a single energy scale for excitations. As a result of these considerations, the Hamiltonian for trimers is up to a constant equivalent to

$$\mathcal{H}_{LI} = -J \sum_{\langle ij \rangle} S_i S_j \,. \tag{3.69}$$

The exchange energy J sets the scale for local excitations and is related to the three interaction energies by

$$J = \frac{1}{4}\Delta E = \frac{1}{4}(E_1 - 2E_2 + E_3). \tag{3.70}$$

Although the energy scales possess the generic ordering $E_1 < E_2 < E_3$, the sign of the exchange coupling J can attain in principle both negative and positive values. For two-dimensional colloidal systems interacting via strongly screened Coulomb interaction explicit evaluation yields positive values, i.e., "ferromagnetic" coupling. For systems with different microscopic interaction, e.g., with paramagnetic particles, it may even be possible to realize an "anti-ferromagnetic" coupling.

For a two-dimensional Lenz-Ising model an exact solution is available for various lattice symmetries (Baxter 1989). On a triangular lattice the transition between the "ferromagnetic" and "paramagnetic" phase occurs at $k_B T_c = 4J/\ln 3$. In the experiments under consideration here (Brunner and Bechinger 2002), the temperature is kept fixed and the intensity of the external potential is varied. This variation is accompanied by the change of the linear extensions

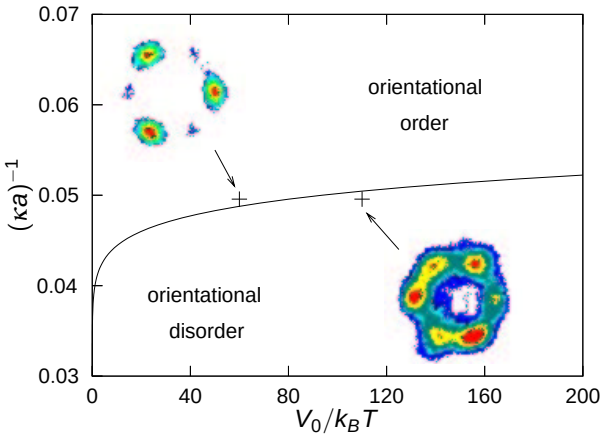

Figure 3.27: Phase diagram of the colloidal trimer system as a function of the strength of the external potential (in units of $k_B T$ where $T = 295\,\mathrm{K}$) and colloid-colloid interaction characterized by a product of the inverse Debye length and the lattice constant (solid line). The two crosses correspond to the experimental observations (Brunner and Bechinger 2002). Insets: averaged local particle densities as represented in Figs. 3.24 (f) and (h).

of trimers, which further affects the strength of the exchange energy J. Above some critical laser intensity the exchange energy becomes smaller than the critical one,

$$J < J_c = k_B T \frac{\ln 3}{4}, \tag{3.71}$$

and the orientational order of the trimer system is lost.

Employing the same parameters (Brunner and Bechinger 2002) as for Fig. 3.24, $\kappa^{-1} = 570\,\text{nm}$ for the inverse screening length, $\mathcal{E}_0 = 3.4 \times 10^4\, k_B T$ for the strength of the screened Coulomb interaction, and $T = 295\,\text{K}$ for the room temperature, Fig. 3.27 shows the phase diagram in the $(V_0/k_B T, (\kappa a)^{-1})$ plane in comparison to the experimental results. In the experiments described above, for $V_0 = 60\, k_B T$ the trimer system is orientationally ordered, whereas it is disordered for $V_0 = 110\, k_B T$. The critical strength of the laser potential found in the theoretical calculations is in striking agreement with these observations, i.e., $V_0^c = 78.6\, k_B T$.

3.4.2 Colloidal dimers on triangular lattices

There is even richer phase behavior for a filling factor $m = 2$. Then, for sufficiently deep substrate potentials, one expects that a defect-free structure is formed where the composite objects in each potential minimum are dimers. For an isolated dimer there are now three different orientational states per lattice site denoted by $\sigma_i = 1, 2, 3$; see Fig. 3.28 (a). As in the case of trimers, the interaction of neighboring dimers is the origin of orientational ordering, whereas the balance of the internal repulsion and the laser pressure yields merely the binding energy of the dimers. From Fig. 3.28 (b) one infers that there are four interaction energies for the 3^2 configurations of neighboring dimers with generic ordering $E_1 < E_2 < E_3 < E_4$. The relation between these model parameters and the experimental control parameters like screening length and potential strength can be worked out in detail (Šarlah et al. 2006), but is far too involved to be presented in this review. As a guidance there are the following trends. Increasing the laser potential compresses the dimers and thus by increasing the effective distances between neighboring dimers reduces their interaction energies, and thus the values of E_i and the spacings between them. This is the basic mechanism underlying orientational melting. Lowering the screening length effectively corresponds to increasing the potential strength.

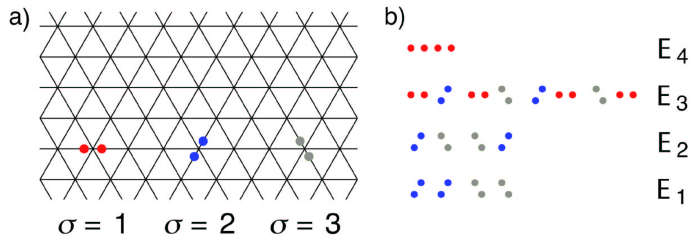

Figure 3.28: Lattice gas model for dimers. (a) The triangular lattice of the external field and the three discrete orientational states of the dimers. (b) Four interaction energies for the orientational configurations of neighboring dimers.

The dependence of the interaction of dimers on the orientation of the bond vector follows from the symmetry of the composite objects, i.e., there are three inequivalent pairs of lattice orientations $\alpha = 1, 2, 3$ corresponding to the three orientational states of the dimers, σ_i. It can be shown (Šarlah et al. 2005; Šarlah et al. 2006) that the interaction Hamiltonian up to an additive constant reduces to (Šarlah et al. 2005; Šarlah et al. 2006)

$$\mathcal{H} = -K \sum_{\langle ij \rangle} \delta_{\sigma_i,\sigma_j} - M \sum_{\alpha=1}^{3} \sum_{\langle ij \rangle_\alpha} \delta_{\sigma_i,\alpha} \delta_{\sigma_j,\alpha} \,, \tag{3.72}$$

where the new energy scales K and M are given in terms of the direct dimer interaction energies by $K = -E_1 + E_2$ and $M = E_1 - 2E_2 + 2E_3 - E_4$. The K-term accounts for the energy gained if two neighboring dimers are in the same orientational state, whereas the M-term distinguishes the high symmetry state of alignment of the dimers with the lattice of the bond vectors. This Hamiltonian is a natural generalization of the Potts model introduced in section 3.2.1.

Comparing the exact ground state energies of different ordered structures, one can infer the possible broken symmetry phase at low temperatures. In total, one finds four ordered phases of different symmetry (Šarlah et al. 2005; Šarlah et al. 2006), see Fig. 3.29. These phases are thermodynamically stable in different regions of the phase diagram, depicted in Fig. 3.30.

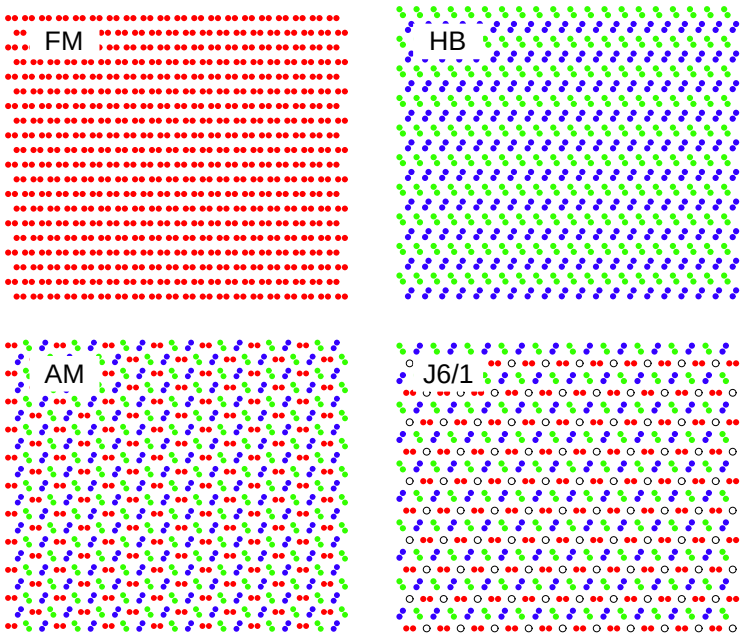

Figure 3.29: Ground state ordered structures of 2d colloidal dimers: ferromagnetic (FM), herring bone (HB), Potts antiferromagnetic (AM), and Japanese 6 in 1 (J6/1), structure. In the latter, the energy of the system does not depend on the orientation of dimers on sites denoted by circles.

In addition to a *ferromagnetic state* (FM), there appears an *antiferromagnetic phase* (AM) stable for $K < 0$ and not too large M. Here, in the fully ordered state, neighboring dimers are in different orientational states. On the triangular lattice this implies that each dimer is surrounded by three neighbors of a configuration rotated by 60° and by three neighbors of a configuration rotated by -60° with respect to the configuration of the central dimer. There are three triangular sublattices with a lattice constant of $a\sqrt{3}$ and the sublattices are equivalent in the sense that each of them can be obtained by a spatial translation with a simultaneous rotation of the dimers of any other one. For positive K and sufficiently negative M a *herring bone* (HB) structure represents the state of lowest free energy, see Fig. 3.29. Statistically equivalent dimers are arranged in two sets of rows, the majority orientational states corresponding to the ones not parallel to the orientation of the rows. Finally, one finds that intervening between the FM and AM for $K < 0$ there appears a phase of four triangular sublattices. Three of them are equivalent in the sense mentioned above, the fourth one exhibiting no preferred orientation, i.e., is in a paramagnetic state. Due to its resemblance to a weaving pattern for chain mailles worn by samurais in the 14th century this phase has been termed *Japanese 6 in 1 phase* (J6/1).

The solid (dashed) straight lines in Fig. 3.30 represent first (second) order phase boundaries as obtained from a mean-field analysis (Šarlah et al. 2005; Šarlah et al. 2006). The basic idea of this analysis is to make an ansatz for the equilibrium density matrix which approximates it by a product of single-site density matrices (Chaikin and Lubensky 1995). The latter are then chosen as to represent the order expected from the ground states as shown in Fig. 3.29.

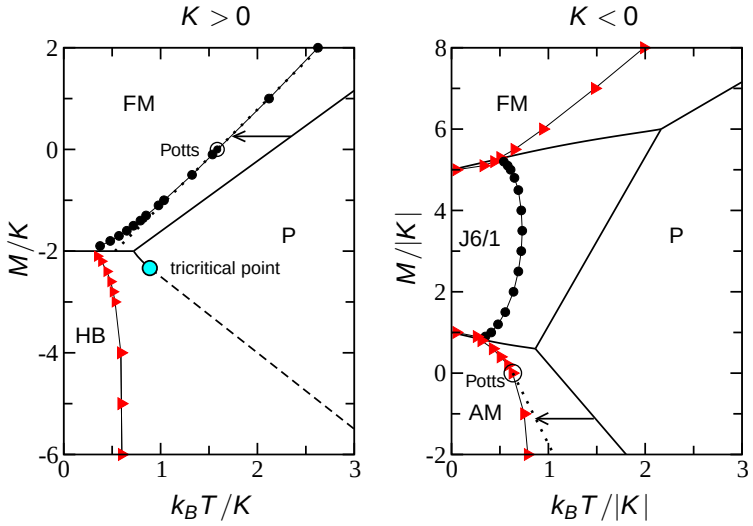

Figure 3.30: Phase diagram for colloidal dimes. Solid lines represent first order transitions derived from the mean-field description and the dashed line after the tricritical point represents the line of second order transitions. Dots and crosses denote the respective continuous and discontinuous transition points as obtained by Monte Carlo simulations; the two encircled symbols indicate the pure Potts transitions. Dotted lines represent the extrapolation of the critical point of the Potts model, see text.

For the ferromagnetic phase the analysis is quite straightforward since the orientational ordering is homogeneous; it is to a large degree identical to the discussion of the Potts model as described in the textbook of Chaikin and Lubensky (Chaikin and Lubensky 1995). For any other phase, the order parameters are spatially varying such that one has to consider a proper set of sublattices for the mean-field analysis which then becomes more involved. Of course, the predictions of the mean-field analysis are not exact, as correlation effects are neglected. Upon inspection of Fig. 3.30, which also shows the results of Monte Carlo simulations (Šarlah et al. 2005; Šarlah et al. 2006), it is evident that mean-field theory still captures the topology of the phase diagram and the main trends in the dependence of the phase boundaries on the control parameters M and K. However, quite generally, mean-field theory overestimates the transition temperatures with respect to the results of Monte Carlo simulations. For the transition between the herringbone and the paramagnetic phase it even seems that the actual phase boundary asymptotes a vertical tangent for large negative values of M. More seriously, some of the phase boundaries become continuous by fluctuation effects. For example, the ferromagnet-paramagnet phase boundary is found to be clearly second order in Monte Carlo simulations, in stark contrast to the mean-field prediction.

3.4.3 Fractional fillings

An even richer variety of phases emerges for fractional fillings m of a triangular lattice (Reichhardt and Reichhardt 2005). For $1 < m < 2$ ground states form where each of the potential minima is either occupied by a colloidal monomer or dimer. Generic values of m lead to orientationally frustrated situations and hence to disordered ground states. Only for a particular set of rational fractions ordered ground states emerge. For example, at $m = 7/4$, star and pinwheel ground states have been observed; see Fig. 3.31.

Which of these phase is the stable ground state was found to depend on the relative strength of the substrate potential. Similar ordering phenomena have also been observed in surface science, where simple linear molecules physisorbed on graphite have been studied quite in-

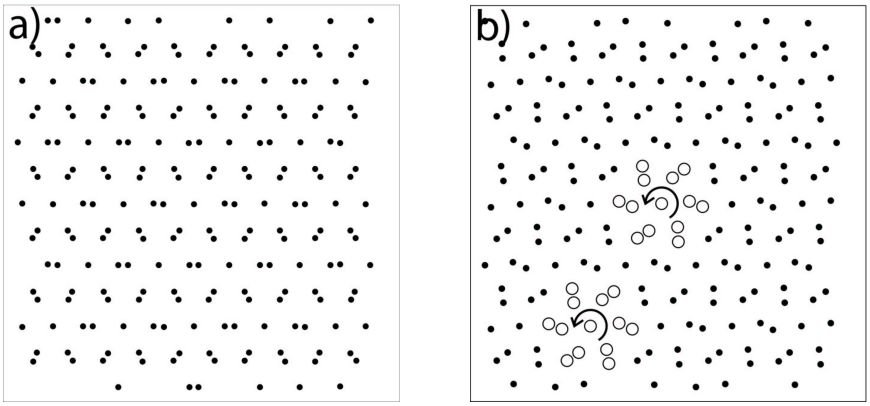

Figure 3.31: Colloidal ground state configurations for filling factor $m = 7/4$: (a) star order, (b) pinwheel order; adapted from the recent article of (Reichhardt and Reichhardt 2005).

tensively (Steele 1996; Marx and Wiechert 1996). Theoretical studies in this area, which have mainly focused on molecules interacting via electric quadrupole interaction (Berlinsky and Harris 1978; Harris and Berlinsky 1979; Mouritsen and Berlinsky 1982; Harris et al. 1984), have enumerated a range of phases including herring bone and pinwheel states. The analogies and differences between these atomic and the soft matter systems have not been fully explored yet. A particular advantage of the soft matter system seems to be that both the substrate potential as well as the colloid-colloid interaction are well characterized. This, at least in principle, makes it feasible to make quantitative theoretical predictions for the phase diagram, similar as discussed in section 3.4.1.

3.5 Commensurate-incommensurate transitions

In the previous section we have discussed commensurate structures, where the periodicity of the adsorbate is a multiple of the lattice constant of the substrate. For thin layers of adsorbate on crystalline surfaces this is not the generic situation. Rather generally one encounters situations, where the adsorbate is strained owing to the lattice mismatch; this may either be different lattice symmetry or lattice constant or even both. Then there is a competition between the adsorbate-adsorbate and the adsorbate-surface interaction. When the substrate potential is dominant, the adsorbed atoms occupy the sites commensurate with the underlying surface. In contrast, if the mutual interactions between the adsorbate atoms dominate, the lattice mismatch will cause incommensurate structures. When these interactions are comparable, an ordered commensurate (C) surface layer can undergo a transition into an incommensurate (IC) phase as a function of some control parameter such as temperature or density.

Already more than 50 years ago it has been suggested by Frank and van der Merwe (Frank and van der Merwe 1949a; Frank and van der Merwe 1949b) that a weakly incommensurate surface layer should be composed of locally commensurate regions separated by a periodic array of discommensurations (domain walls). They have reached this conclusion by considering a one-dimensional model system, where a linear harmonic chain of N particles is subject to a periodic potential, also known as the *Frenkel-Kontorowa model* (Frenkel and Kontorowa 1938)

$$\mathcal{H}_{\text{FK}} = \sum_{n=1}^{N} \left[\frac{1}{2} K (x_{n+1} - x_n - a)^2 - V_0 \cos\left(\frac{2\pi}{b}\, x_n \right) \right] . \tag{3.73}$$

Here a is the period of the free chain, x_n is the coordinate of the nth particle, and K is the stiffness of the spring. At zero temperature the phase diagram of this model is known in detail and shows a multitude of commensurate phases; for a discussion see the textbook of Chaikin and Lubensky (Chaikin and Lubensky 1995) or the monograph by Lyuksyutov et al. (1992). For weak potentials, $V_0 \ll Kb^2$, and small lattice mismatch parameters, $\delta = a - b \ll b$, a continuum limit can be employed. Then one finds that for a window of mismatch parameters, $|\delta| < \delta_c$ with $\delta_c \propto \sqrt{V_0/K}$, the ground state of the chain is in registry with the substrate, but forms large nearly registered domains of size l separated by domain walls of width $\lambda \ll l$ for mismatch parameters slightly outside of this window. These walls are called heavy and light, respectively, if the density in the walls is larger or smaller than in the registered domains. The size of the domain walls scales as $\lambda \propto ab\sqrt{K/V_0}$. Since the separation between these

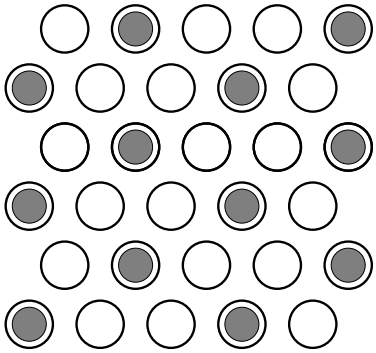

Figure 3.32: Schematic illustration of a commensurate $\sqrt{3} \times \sqrt{3}$ R $30\,\mathrm{deg}$ structure with only $1/3$ of the lattice sites (open circles) occupied with particles (solid circles).

walls diverges logarithmically with $|\delta| - \delta_c$ the difference between the lattice constant of the adsorbate lattice and b goes to zero as $1/\ln\left[(|\delta| - \delta_c)\right]^{-1}$, i.e., the C-IC transition in the Frenkel-Kontorowa model at zero temperature is second order.

The concept of domain walls can readily be extended to two dimensions. The point discommensurations of the 1d model become line defects, which may or may not intersect. Depending on the symmetry of the substrate potential striped arrays of parallel domain walls or networks of hexagons are possible patterns; see e.g. the reviews by Lyuksyutov et al. (1992) and Bak (1981). Here we restrict our attention to one of the best known experimental systems where a C-IC transition has been observed and characterized, namely Krypton monolyers adsorbed on the basal-plane surface of graphite. Krypton occupies one of three sublattices of adsorption sites, which are the graphite hexagon centers. The commensurate structure is a $\sqrt{3}\times\sqrt{3}\,R\,30^\circ$ phase illustrated in Fig. 3.32. Upon increasing the density of adatoms there is a transition into an incommensurate phase, whose nature critically depends on the sign of the domain wall crossing energy $\epsilon_\times$ (Bak et al. 1979). At zero temperature the transition from the commensurate to an incommensurate striped phase was predicted to be of second order, whereas it becomes a first order transition into a hexagonal array of domain walls for negative $\epsilon_\times$. This picture is expected to hold quite generically if the spacing between the domain walls is large compared to the width of the domain walls. It breaks down when these length scales become comparable of finite size effects start to play an important role. Then the precise form of the pair potential and the substrate potential are relevant. Since both of these interactions are known quite well for colloidal systems they are ideal model systems to discuss the ensuing domain patterns. This will be the subject of discussion in section 3.5.1.

The phenomenology of commensurate to incommensurate transitions becomes considerably more complex as soon as thermal fluctuations are taken into account. Then entropic effects due to thermal domain wall wandering in the striped phase (Pokrovsky and Talapov 1979) and "breathing" of the hexagons in the honecomb array of domain walls (Villain 1980) have to be taken into account. The phase behavior is then determined by the interplay between proliferation of domain wall arrays and melting of the domain wall superlattice by a dislocation-mediated mechanism. In particular it has been found that for sufficiently low

commensurability ratios the incommensurate phase is unstable against spontaneous creation of dislocations (Coppersmith et al. 1981; Coppersmith et al. 1982). More recently, similar questions have been asked in the context of vortices in type-II superconductors interacting with periodic pinning arrays; see e.g. the article by Reichhardt et al. (2001) and references cited therein. In contrast to the smooth substrate potentials considered in section 3.4, where each potential minimum may contain a number of particles, the potential landscape of a periodic pinning array is mainly flat inter-dispersed by potential minima which may be occupied by at most one particle. Such potentials can be created by holographic optical tweezer techniques (Dufresne and Grier 1998), allowing for a versatile soft matter model system to study commensurate-incommensurate transitions, which we will discuss in section 3.5.2.

3.5.1 Strain-induced domain formation in adsorbed monolayers

Colloidal systems offer a unique set of advantages to study domain formation in adsorbed monolayers. First, one can clearly distinguish between pure strain effects and system specific interactions. Second, the lattice mismatch and other system parameters can be varied independently over large ranges. Third, since the interparticle potential is well known, the elastic energies in colloidal systems which are the driving force for domain formation can be directly calculated.

Fig 3.33 shows typical configurations of a 2d colloidal suspension of charge-stabilized polystyrene spheres of $2.8\,\mu$m diameter on a light-induced (111) surface with lattice constant $b = 5.5\,\mu$m (Bleil et al. 2006). Without the light pattern and with the particle number densities considered here, the colloids form a fluid with the mean particle distance a. The lattice mismatch between the colloidal monolayer and the substrate is characterized by the filling factor $\eta = (\frac{b}{a})^2$ which can be continuously changed by variation of the particle density with a boundary box created with a scanning optical tweezer. Fig. 3.33 shows typical equilibrated configurations of colloids on a light-induced (111) surface with potential strength $V_0 = 6.9 k_B T$ for different values of η. For $\eta = 0.34$ the colloids form over large areas hexagonal structures

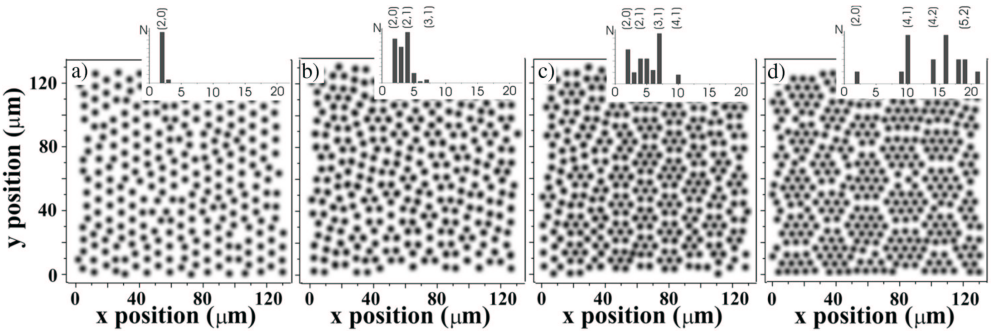

Figure 3.33: Colloidal particles on a triangular light field for $V_0 = 6.9 k_B T$ for $\eta = 0.34$ (a), 0.48 (b), 0.59 (c) and 0.69 (d). To enhance the visibility of the domain walls, the snapshots are artificially defocused. Histograms in the inset figures quantify the relative occurrence of particle numbers belonging to a single domain (Bleil et al. 2006).

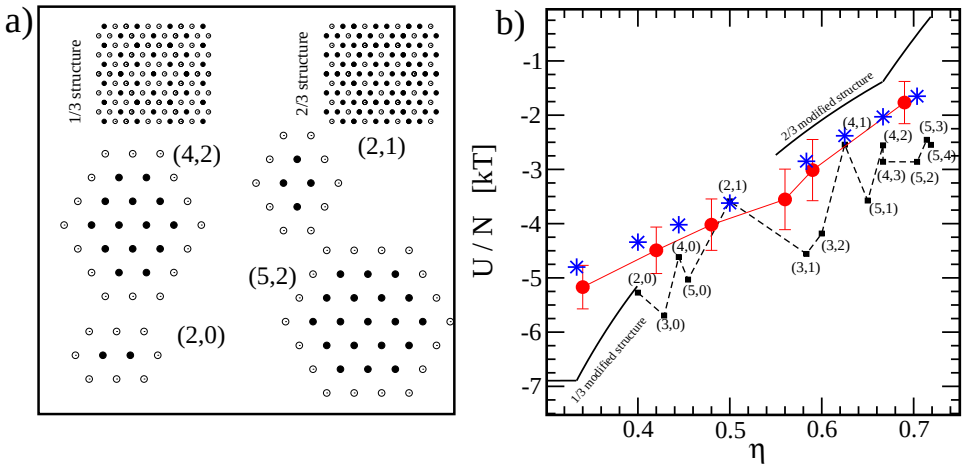

Figure 3.34: a) Possible structures of colloids (solid circles) on triangular substrates (open circles) for different η. The notation for the cluster structures (nn, n_j) is explained in the text. b) Energy per particle vs. η for $V_0 = 6.9\,k_BT$: Experimental data (closed circles), Monte Carlo simulations (stars) and theoretically calculated for various area-filling, relaxed domain structures (filled squares with dashed lines as guide to the eye) (Bleil et al. 2006).

with a lattice constant $\sqrt{3}\,b$ and rotated by $30°$ with respect to the substrate lattice (Fig. 3.33 a). This structure corresponds to the $\sqrt{3} \times \sqrt{3}$R30° triangular commensurate lattice predicted for $\eta = \frac{1}{3}$ and is schematically shown in the upper left inset of Fig. 3.34. Increasing η to 0.48, 0.59 and 0.69 leads to the formation of *domain* structures, i.e., regularly formed particle clusters which becomes increasingly pronounced at higher η (Figs. 3.33 b,c,d). Here, a domain is defined as a cluster of particles, placed on next neighbor lattice sites, with two of these clusters being separated from each other by *domain walls*, i.e. single rows of unoccupied sites. The insets in Fig. 3.33 show histograms of the particle numbers comprising the clusters. Although the particle interaction is short-ranged, the domain walls form a rather regular network with the average domain size increasing with growing η. Since the particle density inside domains is slightly above the average particle density, domain formation requires - in addition to the repulsive particle interaction - effective attractive forces. The origin of these forces is due to the elastic energy between the colloidal monolayer and the substrate as will be discussed next.

The energy U of the colloidal system is given by

$$U = \sum_{i<j} \Phi(r_{ij}) + \sum_i V(x_i, y_i) \tag{3.74}$$

with r_{ij} and (x_i, y_i) being the particle distances and their positions, respecitvely. The two terms account for the pair potential, Eq. 3.55, and the interaction of the colloids with the substrate

$$V(x,y) = -\frac{2}{9}V_0 \left\{ \frac{3}{2} + \cos\left(\frac{4\pi y}{\sqrt{3}b}\right) + 2\cos\left(\frac{2\pi y}{\sqrt{3}b}\right)\cos\left(\frac{2\pi y}{b}\right) \right\}. \tag{3.75}$$

With the experimentally determined Debye screening length $\kappa^{-1} = 580 \pm 60$nm and the effective charge $Z^* \approx 5400$ one obtains the energy per particle U/N from the experimentally obtained particle positions. The closed circles in Fig. 3.34 b show the results for different η which are in excellent agreement with the results of Monte Carlo simulations (star-symbols in Fig. 3.34 b), which were performed for the same conditions as in the experiments (Bleil et al. 2006).

More information about domain formation is gained by analyzing those particle configurations which minimize Eq. 3.74. The structures most frequently observed in simulations and experiments are symmetrically shaped clusters, which can be characterized by $2n_J + 1$ rows, nn particles in the central row, $(nn - 1)$ particles in the adjacent rows and so forth; for examples see Fig. 3.34. In the following these clusters are referred to as (nn, n_J)-clusters. Together with the empty sites surrounding them, these clusters form characteristic domains which allow the substrate to be completely covered with filling factor

$$\eta = \frac{2\left[nn(1+2n_J) - n_J(n_J+1)\right]}{(n_J+1)[4(nn+2) - 4 - 2(n_J+1)]}\,. \tag{3.76}$$

To study, how such symmetric domain types (at their respective filling factor) relax in the presence of a triangular substrate potential one can perform Langevin simulations. The corresponding energies are also plotted in Fig. 3.34 as closed squares. Indeed, the calculated energies are close to the experimental values and also show the same trend as a function of the filling factor.

From Fig. 3.34 one obtains also the most probable cluster type at given η: The smallest possible cluster is the (2,0) cluster, forming an area-filling structure at $\eta = 0.4$. This is consistent with the experimental observation that at $\eta = 0.34$ almost only (2,0) clusters are found; the (nn, n_J) notation is added to the respective bars in the histograms of Fig. 3.33. At $\eta = 0.48$ and $\eta = 0.59$ the most probable clusters are predicted to be $(2, 1)$ and $(3, 1)$ which is again consistent with experimental data at those values of η (Bleil et al. 2006). At even higher η the correspondence is less obvious, however, Fig. 3.33d supports the trend as predicted from the simulation data in Fig. 3.34 of growing cluster sizes with increasing η. Starting from the $\sqrt{3} \times \sqrt{3}$R30° commensurate phase at $\eta = \frac{1}{3}$ one can also construct other phases at $\eta > \frac{1}{3}$ and $\eta < \frac{1}{3}$ by adding or removing colloids to unoccupied and occupied sites, respectively. If the neighboring added and removed colloids are allowed to adjust within their substrate potential wells to relax their elastic strain, the energy per particle corresponds to the solid line labeled *1/3 modified structure* in Fig. 3.34 (determined via Langevin simulations). The solid line labeled *2/3 modified structure* shows the corresponding results for values of $\eta \approx \frac{2}{3}$. The energy of the $\sqrt{3} \times \sqrt{3}$R30° structure is below the experimental data point at $\eta = 0.34$ and indeed Fig. 3.33 a is essentially a mixture of the $\sqrt{3} \times \sqrt{3}$R30° structure and $(2, 0)$ clusters.

To understand why domain formation becomes energetically more favorable compared to a more uniform surface coverage we exemplarily discuss the situation for $\eta = \frac{2}{3}$. Here the homogeneous $2/3$ structure competes with $(4, 2)$ and $(4, 3)$ domain phases which can be realized at the same filling factor; see Fig. 3.34. Without relaxation effects and only considering next neighbor interactions (which is valid for the short-ranged particle interaction considered here) the homogeneous $2/3$ structure has the smallest energy per particle, i.e., $U/N = 1.5\,\Phi(a)$,

compared to 29 bonds per 14 particles, i.e. $U/N = 29/14\,\Phi(a)$ and $33/16\,\Phi(a)$ for the $(4,2)$ and $(4,3)$ domain phases, respectively. However, while due to symmetry the particles in the $2/3$ structure are fixed to the centers of their lattice sites, the empty sites constituting the domain walls allow the clusters in the $(4,2)$ and $(4,3)$ domains to efficiently relax the elastic strain, such that the domain structures become energetically more favorable than the homogeneous phase; see Fig. 3.34. This clearly demonstrates that the domain formation is favored over the homogeneous phase because of its efficient way to release the elastic stress within the clusters.

It should be mentioned that in case of very large substrate strengths ($V_0^g > 42\,k_BT$) relaxation effects play hardly any role, and the domain structure should become energetically less favorable compared to a homogeneous $2/3$ phase; see upper right inset of Fig. 3.34. This is in agreement with results of Reichhardt et al. (2001), where the $2/3$ structure was predicted to be the ground state for $\eta = 2/3$ in the limit of infinite substrate strength. This clearly demonstrates that it is not only the lattice mismatch between the adsorbate and the substrate but also the substrate strength which eventually determines the resulting morphology of adsorbed monolayers on patterned substrates.

Besides fundamental interest, domain formation plays an important role for the creation of self-organized structures in atomic systems. In those situations, however, it is often not easy to distinguish between pure strain effects and material specific interactions. As we have seen in this section, colloidal systems respond rather similar to incommensurate substrates and thus can also address fundamental questions in this context.

3.5.2 Periodic pinning potentials

Colloidal soft matter also provides versatile model systems to study the interplay between the elasticity of a 2d solid and various types of pinning potentials. For example, they may mimic analogous situations in the mixed phase of type-II superconductors where vortices are interacting with periodic pinning arrays (Martín et al. 1997; Martín et al. 1999). The pinning potential in the colloidal system can be created by a holographic optical tweezer technique (Dufresne and Grier 1998); Fig. 3.35 shows a square array of 9×9 about Gaussian light dots. Since the potential width of about $5\,\mu$m is comparable to the particle size and much smaller than the mean particle distance each pinning site is acting only to a single colloidal particle. This is in contrast to the discussion in section 3.4 where several particles were localized at each potential minimum such that colloidal molecules could form.

Using superparamagnetic colloids (Bubeck et al. 1998; Zahn et al. 1997) allows to study the effect of both the substrate strength and the pair interaction on the domain pattern (Mangold et al. 2003). Then the pair interaction can be adjusted with an external magnetic field B,

$$\Phi_{ij} = \frac{\mu_0}{4\pi}\,\frac{M^2(B)}{r_{ij}^3}\,, \tag{3.77}$$

where r_{ij} is again the distance between particle i and j and $M(B)$ given by the Langevin function (Bubeck et al. 1998; Zahn et al. 1997). The strength of the interaction is then

conveniently measured in terms of the a dimensionless plasma parameter

$$\Gamma = \frac{V_{\text{mag}}}{k_B T} = \frac{\mu_0 M^2 (\pi\rho)^{3/2}}{4\pi k_B T}\,, \tag{3.78}$$

where ρ is the particle number density. Accordingly, the magnetic field plays the role of an inverse effective temperature.

Figs. 3.36 a-f show particle trajectories (left) and averaged local particle densities (right) for superparamagnetic particles of 4.6μm diameter on a square lattice with pinning strength $V_0 = 4.9\, k_B T$ at filling factor $m \approx 4$ as a function of decreasing plasma parameter. At high magnetic fields ($\Gamma = 65.3$) the colloidal pair interaction largely exceeds the interaction with the substrate potential. Accordingly the structure is expected to be close to a triangular lattice as seen in Fig. 3.36 a. For comparison we note that on a flat surface crystallization takes place above $\Gamma = 56.5$ (Zahn et al. 1999). A closer analysis, however, yields small deviations from an ideal triangular lattice by about 6% (regarding the length of the lattice vectors) which are due to the influence of the substrate potential. To minimize the free energy in the presence of the two competing interactions, the system responds by the alignment of a lattice vector of the colloidal crystal along one of the lattice vectors of the substrate potential (Figs. 3.36 a,b). While the periodicity of the substrate is commensurate with the particle spacing in horizontal direction in Fig. 3.36 a, there is a lattice mismatch in vertical direction. On average only each second row of pinning sites is occupied with particles. Obviously, the interaction energy between the colloidal particles is to high, to allow the system to lock to the periodicity of the substrate potential and a floating or *incommensurate* solid is formed. At $\Gamma = 37.6$ the colloidal system is soft enough to allow its geometry to accommodate to that of the substrate lattice. As shown in Figs. 3.36 c,d all the pinning sites are now occupied with a colloidal particle, i.e., the monolayer has partially adopted the square symmetry of the substrate. This

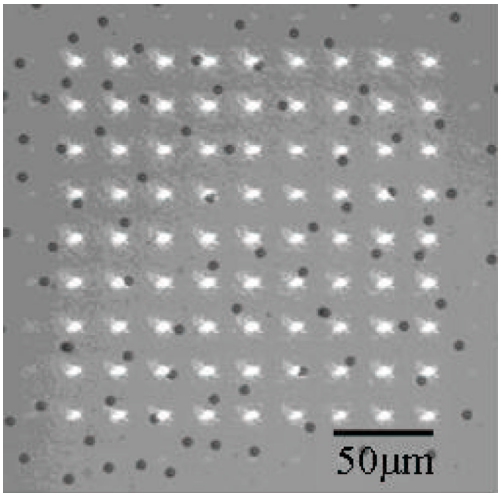

Figure 3.35: Photograph of a square 9×9 patterned holographic tweezer array (bright spots) and colloidal particles (dark objects) (Mangold et al. 2003).

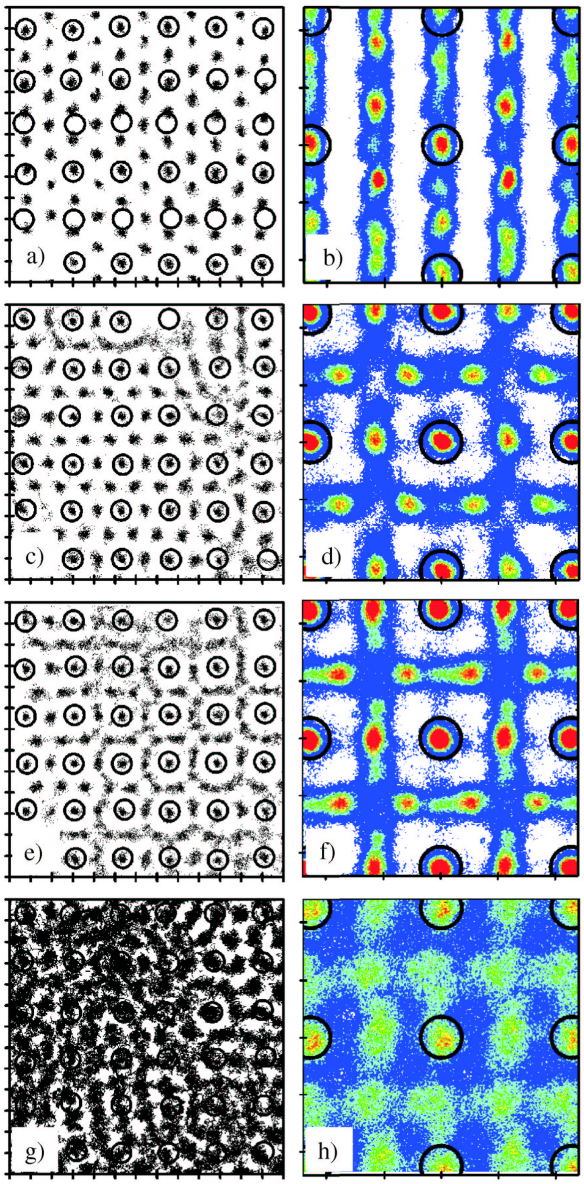

Figure 3.36: Particle trajectories and contour plots for averaged local particle densities for $m = 4$ at different Γ and V_0, respectively. (a),(b) $\Gamma = 65.3$, $V_0 = 4.9\,k_BT$; (c),(d) $\Gamma = 37.6$, $V_0 = 4.9\,k_BT$; (e),(f) $\Gamma = 36.2$, $V_0 = 4.9\,k_BT$; (g),(h) $\Gamma = 23.5$, $V_0 = 1.5\,k_BT$; The pinning sites are marked with open circles. The axis ticks correspond to $10\,\mu$m in all figures.

phenomenology is consistent with the results of Langevin simulation performed for interacting vortices in 2d (Reichhardt et al. 2001).

Further decrease of the particle interaction to $\Gamma = 36.2$ was found to lead to melting of the interstitial particles while the particles at the pinning sites were still highly localized (Figs. 3.36 e, f). The trajectories of the interstitial particles are constrained to a square-like grid which exclude the region around the pinning sites. This is due to the repulsive dipole-interaction of the particles. A similar behavior has also been reported for vortex melting in periodic pinning arrays (Reichhardt et al. 2001). When both, the strength of the particle interaction and the substrate pinning were further decreased ($\Gamma = 23.5$, $V_0 = 1.5 k_B T$), the particles at the pinning sites also become mobile and the entire lattice is in a liquid state as shown in Figs. 3.36 g,h.

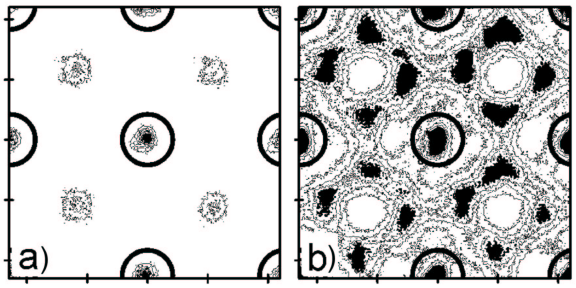

Figure 3.37: Contour plots of averaged particle densities of crystalline structures for filling factors (a) $m \approx 2$ and (b) $m \approx 5.5$. The pinning sites are marked with open circles. The axis ticks correspond to $10\,\mu$m in both figures.

Even more complex structures can be obtained for other filling factors m as shown in Fig. 3.37 a, where the averaged local density of the commensurate crystalline phase for $m \approx 2$, $V_0 = 9.5\,k_B T$, and $\Gamma = 35$ is plotted. Here, the interstitial colloids are localized in the centers between the substrate lattice sites, and the colloids form a centered (1×1) super lattice. For $m = 5.5$ the averaged local particle density of the interstitial particles is plotted for $V_0 = 6.4\,k_B T$ and $\Gamma = 44.4$ in Fig. 3.37 b. In contrast to Fig. 3.37 a, the particle density is almost zero at those positions where the interstitial particles were localized in Fig. 3.37 a. Now, the colloids are arranged in a square-like geometry around these depletion zones. Because $m = 5.5$ deviates slightly from perfect matching conditions, i.e. $m = 5$, the localization of the interstitial particles is less pronounced and defect particles can diffuse along a square-like network across the sample.

In general, the qualitative melting behavior is rather independent of m. According to numerical simulations for vortices in superconductors (Reichhardt et al. 2001; Laguna et al. 2001), however, this is only true for square pinning potentials. In case of triangular and Kagomé lattices and in case of non-integer m values some particles (vortices) start to rotate around pinning sites. As m is further increased (away from an integer value) the number of such ring excitations increases. Experimentally, triangular and Kagomé lattices can be generated by means of holographic gratings or interference patterns, and it will be an interesting question whether such a particle rotation can be also observed in colloidal systems.

3.6 Summary and outlook

In this chapter we have summarized experimental and theoretical studies on the phase behavior of two-dimensional monolayers on patterned substrates. As for smooth substrates, where colloidal model systems are ideal candidates for testing basic ideas of the defect-mediated melting theories (see chapter 2 of this volume by von Grünberg, Keim and Maret), they are also versatile model in case of periodic substrate potentials as they are typically present when considering realistic substrates composed of atoms or molecules. Substrate potentials for colloidal monolayers can be created by extended optical light fields which exert optical forces onto colloidal particles. Compared to atomic crystalline substrates such light-induced surfaces are much more flexible with respect to symmetry, lattice constant and the substrate strength which can be continuously varied. Due to the interplay between interactions amongst the colloids and those with the substrate, there is a competition between different length scales and symmetries. As a result, one finds a rather rich phenomenology with an abundant variety of phases which is observed both in theory as well as in experiments.

If constrained to two dimensions the phase behavior of systems with a continuous and a discrete symmetry of the order parameter is quite distinct. Whereas there are phase transitions into low temperature phases with long range order for systems with discrete symmetries, such transitions are not allowed for systems with continuous symmetries. The latter exhibit an intriguing set of phenomena, such as low temperature phases with quasi-long-range order or phase transitions mediated by the unbinding of topological defects. Colloidal systems with patterned substrates have provided a fresh look on the physics of phase transitions in two dimensions. Subjecting colloidal solids to patterns with a one-dimensional periodicity, one was able to create a system with a symmetry intermediate between continuous and discrete. We have seen that this leads to a state of matter which has been termed a locked floating solid due to his “hybrid” nature of being both locked and freely floating with respect to the substrate. Depending on the degree of commensurability between the colloidal lattice and the substrate, it has been shown theoretically and partly already confirmed experimentally that there are numerous scenarios of melting. It may either proceed directly from a floating solid to a modulated liquid mediated by the unbinding of one particular set of dislocations, or there may be several intermediate phases such as floating solids or locked and floating smectics. Substrate potentials with two-dimensional periodicity have been a rich playground for understanding phase behavior of systems with discrete symmetries. In particular, we have illustrated that one may create molecular colloidal systems which condense into exotic ordered phases such pinwheel, herringbone or even a phase termed “Japanese 6 in 1 phase” since it resembles the weaving pattern for chain mailles worn by samurais in the 14th century.

After having investigated the phase behavior on crystalline surfaces, it will be interesting to study the behavior of monolayers on quasi-crystalline substrates. This issue has recently attracted considerable attention, because there is growing technological interest in using quasi-crystalline substrates as templates for the pseudomorphic growth of deposited adsorbates (Curtarolo et al. 2005) First experiments with monolayers of metals and rare gases indicate a strong dependence of the substrate strength on the structure of the adsorbate (McGrath et al. 2002). In this context, colloidal model systems are again a promising alternative approach.

There are many other interesting questions which may be addressed by colloidal monolayers. One might ask for the effect of different types of disorder, which may be purpose tailored

by holographic optical tweezer techniques. Also combinations of periodic potentials and random pinning potentials are conceivable. From a theoretical viewpoint, it may be interesting to study colloidal mixtures or macromolecular assemblies on patterned surfaces. Finally, yet another open issue are dynamical aspects of monolayers on crystalline surfaces.

Acknowledgements. We would like to express our thanks to all our colleagues and collaborators who have shaped our thinking on soft matter systems, particularly Jörg Baumgartl, Stefan Bleil, Matthias Brunner, Thomas Franosch, Henning v. Grünberg, Paul Leiderer, Konrad Mangold, David Nelson, Leo Radzihovsky, Andreja Šarlah, and Qi-Huo Wei. We would also like to thank Marta Balbás Gambra, Johannes Nold, and Andreja Šarlah for carefully reading the manuscript, and Johannes Nold in addition for his assistance with numerous technical problems in preparing the manuscript.

Bibliography

Agra, R., van Wijland, F., and Trizac, E., 2004, *Phys. Rev. Lett.* **93**, 018304.

Ashkin, A., 1970, *Phys. Rev. Lett.* **24**, 156.

Baert, M., Metlushko, V. V., Jonckheere, R., Moshchalkov, V. V., and Bruynseraede, Y., 1995, *Phys. Rev. Lett.* **74**(16), 3269.

Bak, P., 1981, *Rep. Prog. Phys* **45**, 587.

Bak, P., Mukamel, D., Villain, J., and Wentowska, K., 1979, *Phys. Rev. B* **19**, 1610.

Baumgartl, J. and Bechinger, C., 2005, *Europhys. Lett.* **71**, 487.

Baxter, R. J., 1973, *J. Phys. C* **6**, L445.

Baxter, R. J., 1989, *Exactly solved models in statistical mechanics*. Academic Press, London.

Bechinger, C., Brunner, M., and Leiderer, P., 2001, *Phys. Rev. Lett.* **86**, 930.

Bechinger, C., Wei, Q. H., and Leiderer, P., 2000, *J. Phys.: Condens. Matter* **12**, A425.

Berezinskii, V., 1971a, *Sov. Phys. JETP* **34**, 610.

Berezinskii, V., 1971b, *Sov. Phys. JETP* **32**, 493.

Bergman, D. and Halperin, B., 1976, *Phys. Rev. B* **13**, 2145.

Berlinsky, A. J. and Harris, A. B., 1978, *Phys. Rev. Lett.* **40**, 1579.

Birgeneau, R. and Horn, P., 1986, *Science* **232**, 329.

Bleil, S., Grünberg, H., Dobnikar, J., Castaneda-Priego, R., and Bechinger, C., 2006, *Europhys. Lett.* **73**, 450.

Bloch, I., 2005, *Nature Physics* **1**, 23.

Brunner, M. and Bechinger, C., 2002, *Phys. Rev. Lett.* **88**, 248302.

Brunner, M., Bechinger, C., Strepp, W., Lobaskin, V., and von Grnberg, H. H., 2002, *Europhys. Lett.* **58**, 926.

Bubeck, R., Nesser, S., Bechinger, C., and Leiderer, P., 1998, *Progr. Colloid Polym. Sci.* **110**, 41.

Burns, M., Fournier, J.-M., and Golovchenko, J., 1990, *Science* **249**, 749.

Chaikin, P. M. and Lubensky, T. C., 1995, *Principles of condensed matter physics*. Cambridge University Press, Cambridge.

Chakrabarti, J., Krishnamurthy, H. K., and Sood, A. K., 1994, *Phys. Rev. Lett.* **73**, 2923.

Chakrabarti, J., Krishnamurthy, H. R., Sood, A. K., and Sengupta, S., 1995, *Phys. Rev. Lett.* **75**, 2232.

Chaudhuri, D. and Sengupta, S., 2004a, *Europhys. Lett.* **67**, 814.

Chaudhuri, D. and Sengupta, S., 2004b, *Europhys. Lett.* **68**, 160.

Chaudhuri, D. and Sengupta, S., 2006, *Phys. Rev. E* **73**, 011507.

Chowdhury, A., Ackerson, B. J., and Clark, N. A., 1985, *Phys. Rev. Lett.* **55**, 833.

Coppersmith, S., Fisher, D., Halperin, B., Lee, P., and Brinkman, W., 1982, *Phys. Rev. B* **25**, 349.

Coppersmith, S. N., Fisher, D. S., Halperin, B. I., Lee, P. A., and Brinkman, W. F., 1981, *Phys. Rev. Lett.* **46**, 549.

Curtarolo, S., Setyawan, W., Ferralis, N., Diehl, R., and Cole, M., 2005, *Phys. Rev. Lett.* **95**, 136104.

Das, C., Chaudhuri, P., Sood, A., and Krishnamurthy, H., 2001, *Curr. Sci.* **80**, 959.

Das, C., Krishnamurthy, H., Sood, A., and Sengupta, S., 1998, *Phys. Rev. B* **58**, R5889.

Das, C., Sood, A., and Krishnamurthy, H., 1999, *Physica A* **270**, 237.

de Gennes, P., 1974, *The Physics of Liquid Crystals*. Clarendon Press, London.

Derjaguin, B. V. and Landau, L., 1941, *Acta Physicochim. USSR* **14**, 633.

Dufresne, E. and Grier, D., 1998, *Rev. Sci. Instrum.* **69**, 1974.

Escuti, M. J. and Crawford, G. P., 2004, *Opt. Eng.* **43**, 1973.

Fisher, D., Halperin, B., and R.Morf, 1979, *Phys. Rev. B* **20**, 4692.

Frank, F. and van der Merwe, J., 1949a, *Proc. R. Soc. (London) Ser. A* **198**, 205.

Frank, F. and van der Merwe, J., 1949b, *Proc. R. Soc. (London) Ser. A* **198**, 216.

Frenkel, Y. and Kontorowa, T., 1938, *Zh. Eksp. Teor. Fiz.* **8**, 1340.

Frey, E., Nelson, D. R., and Radzihovsky, L., 1999, *Phys. Rev. Lett.* **83**, 2977.

Grier, D., 2003, *Nature* **424**, 810.

Halperin, B. I. and Nelson, D. R., 1978, *Phys. Rev. Lett.* **41**, 121.

Harris, A. and Berlinsky, A., 1979, *Can. J. Phys.* **57**, 1852.

Harris, A., Mouritsen, O., and Berlinsky, A., 1984, *Can. J. Phys.* **62**, 915.

Helden, L., Roth, R., Koenderink, G., Leiderer, P., and Bechinger, C., 2003, *Phys. Rev. Lett.* **90**, 48301.

Huang, K., 1987, *Statistical Mechanics*. Wiley, New York.

Israelachvili, J., 1985, *Intermolecular & Surface Forces*. Academic Press, London.

Jancovici, B., 1967, *Phys. Rev. Lett.* **19**, 20.

José, J., Kadanoff, L., Kirkpatrick, S., and Nelson, D., 1977, *Phys. Rev. B* **16**, 1217.

Kerker, M., 1969, *The scattering of light*. Academic Press, New York.

Kosterlitz, J. M. and Thouless, D. J., 1972, *J. Phys. C* **5**, L124.

Kosterlitz, J. M. and Thouless, D. J., 1973, *J. Phys. C* **6**, 1181.

Laguna, M. F., Balseiro, C. A., Domínguez, D., and Nori, F., 2001, *Phys. Rev. B* **64**(10), 104505.

Landau, L. D., 1937, *Fiz. Z. Sowejetunion* **11**, 26.

Leunissen, M., Christova, C., Hynninen, A.-P., Royall, C., Campbell, A., Imhof, A., Dijkstra, M., van Roij, R., and van Blaaseren, A., 2005, *Nature* **437**, 235.

Likos, C. N., 2001, *Phys. Rep.* **348**, 267.

Lin, K. H., Crocker, J. C., Prasad, V., Schofield, A., and Weitz, D. A., 2000, *Phys. Rev. Lett.* **85**, 1770.

Loudiyi, K. and Ackerson, B. J., 1992, *Physica* **184A**(1-2), 1.

Löwen, H., 1994, *Phys. Rep.* **237**, 249.

Lyuksyutov, I. F., Naumovets, A. G., and Pokrovsky, V. L., 1992, *Two-dimensional crystals*. Academic Press, Boston.

Mangold, K., Leiderer, P., and Bechinger, C., 2003, *Phys. Rev. Lett.* **90**, 158302.

Martín, J., Vélez, M., Hoffmann, A., Schuller, I., and Vicent, J., 1999, *Phys. Rev. Lett.* **83**, 1022.

Martín, J. I., Vélez, M., Nogués, J., and Schuller, I. K., 1997, *Phys. Rev. Lett.* **79**, 1929.

Marx, D. and Wiechert, H., 1996, in *Advances in Chemical Physics*, edited by I. Prigogine and S. Rice, vol. 95, p. 213. John Wiley, New York.

Matsuda, T., Harada, K., Kasai, H., Kamimura, O., and Tonomura, A., 1996, *Science* **271**, 1393.

McGrath, R., Ledieu, J., Cox, E., and Diehl, R., 2002, *J. Phys.: Condens. Matter* **14**, R119.

Mermin, N. D. and Wagner, H., 1966, *Phys. Rev. Lett.* **17**, 1133.

Morf, R., 1979, *Phys. Rev. Lett.* **43**, 931.

Mouritsen, O. and Berlinsky, A., 1982, *Phys. Rev. Lett.* **48**, 181.

Nelson, D., 2002, *Defects and Geometry in Condensed Matter Physics*. Cambridge University Press.

Nelson, D. R. and Halperin, B. I., 1979, *Phys. Rev. B* **19**, 2457.

Onsager, L., 1944, *Phys. Rev.* **65**, 117.

Ostlund, S. and Halperin, B., 1981, *Phys. Rev. B* **23**, 335.

Peierls, R., 1935, *Ann. Inst. Henri Poincaré* **5**, 177.

Pokrovsky, V. and Talapov, A., 1979, *Phys. Rev. Lett.* **42**, 65.

Pokrovsky, V. L., 1986, in *Solitons*, edited by E. E. Trullinger, V. E. Zakharov, and V. L. Pokrovsky, vol. 17 of *Modern Problems in Condensed Matter Sciences*. North-Holland, Amsterdam.

Pusey, P. N. and van Megen, W., 1986, *Nature* **320**, 340.

Radzihovsky, L., Frey, E., and Nelson, D. R., 2001, *Phys. Rev. E* **63**, 031503.

Reichhardt, C. and Olson, C. J., 2002, *Phys. Rev. Lett.* **88**, 248301.

Reichhardt, C., Olson, C. J., Scalettar, R. T., and Zimányi, G. T., 2001, *Phys. Rev. B* **64**(14), 144509.

Reichhardt, C. and Reichhardt, C. J. O., 2005, *Phys. Rev. E* **71**, 062403.

Russel, W. B., Seville, D. A., and Schowalter, W. R., 1995, *Colloidal dispersions*. Cambridge University Press, Cambridge.

Schick, M., 1981, *Progress in Surface Science* **11**, 245.

Sengupta, S., Nielaba, P., and Binder, K., 2000a, *Europhys. Lett.* **50**, 668.

Sengupta, S., Nielaba, P., and Binder, K., 2000b, *Phys. Rev. E* **61**, 6294.

Sinha, S. (ed.), 1980, *Ordering in Two Dimensions*. North-Holland, New York.

Steele, W., 1996, *Langmuir* **12**, 145.

Strepp, W., Sengupta, S., and Nielaba, P., 2001a, *Phys. Rev. E* **63**, 046106.

Strepp, W., Sengupta, S., and Nielaba, P., 2001b, *Phys. Rev. E* **66**, 056109.

Toner, J. and Nelson, D., 1981, *Phys. Rev. B* **23**, 316.

van Blaaderen, A., Ruel, R., and Wiltzius, P., 1997, *Nature* **385**, 321.

Vervey, E. J. W. and Overbeek, J. T. G., 1948, *Theory of the stability of lyophobic colloids*. Elsevier, Amsterdam.

Villain, J., 1980, in *Ordering in Strongly Fluctuating Condensed Matter Systems*, edited by T. Riste, p. 221. Plenum Press, New York.

Visscher, K., Gross, S., and Block, S., 1996, *IEEE J. Quantum Electron.* **2**, 1066.

Vollmayr, H., 1992, *Phys. Rev. B* **46**, 733.

Šarlah, A., Franosch, T., and Frey, E., 2005, *Phys. Rev. Lett.* **95**, 088302.

Šarlah, A., Frey, E., and Franosch, T., 2006, *Phys. Rev. E* **??**, ????

Wegner, F., 1967, *Z. Phys.* **206**, 465.

Wei, Q.-H., Bechinger, C., Rudhardt, D., and Leiderer, P., 1998, *Phys. Rev. Lett.* **81**, 2606.

Wu, F. Y., 1982, *Rev. Mod. Phys.* **54**, 235, and the references here-in.

Young, A. P., 1979, *Phys. Rev. B* **19**, 1855.

Zahn, K., Lenke, R., and Maret, G., 1999, *Phys. Rev. Lett.* **82**, 2721.

Zahn, K., Méndez-Alcaraz, J. M., and Maret, G., 1997, *Phys. Rev. Lett.* **79**, 175.

Index